



Evolution of size and composition of fine particulate matter in the Delhi megacity during later winter

Navaneeth Meena Thamban^a, Vipul Lalchandani^a, Varun Kumar^b, Suneeti Mishra^a,
Deepika Bhattu^{b,d}, Jay G. Slowik^b, Andre S.H. Prevot^{b,**}, Rangu Satish^c, Neeraj Rastogi^c,
Sachchida N. Tripathi^{a,e,*}

^a Department of Civil Engineering, Indian Institute of Technology, Kanpur, India

^b Laboratory of Atmospheric Chemistry, Paul Scherrer Institute, Forschungsstrasse 111, 5232 Villigen, Switzerland

^c Geosciences Division, Physical Research Laboratory, Ahmedabad, 380009, India

^d Currently at Department of Civil and Infrastructure Engineering, Indian Institute of Technology, Jodhpur, 342037, Rajasthan, India

^e Centre for Environmental Science and Engineering, Indian Institute of Technology, Kanpur, India

HIGHLIGHTS

- Amines, chloride, and hydrocarbon like OA (HOA) show similar diurnal growth and possibilities of internal mixing in Delhi.
- HOA, families of hydrocarbon (CH), and amines and chloride grow prominently up to a diameter of ~900 nm during the photochemically active period.
- Secondary OA (SOA) significantly promotes the growth of primary OA sources, OA families, and inorganics such as chloride and nitrate.
- Sampling sites in Delhi show a significant difference in size-resolved acidity that governs the growth of species.
- For an increase in the mass fraction of 0.1 SOA in OA, the sizes of HOA, chloride, primary amines (CHN family), and secondary amines (CHON family) are increased up to ~93, 80, 66, and 47 nm, respectively in Delhi.
- Condensation of photochemically produced SOA is important in determining the growth of aerosols in late winter in Delhi.

ARTICLE INFO

Keywords:
HR-PTof
Organic aerosol
Size
Composition
Evolution

ABSTRACT

This study presents the first multi-site evolution analysis of fine Organic Aerosols (OA) and inorganics in the Delhi megacity (National Capital Region (NCR)) using high-resolution-particle time of flight (HR-PTof) size distribution obtained from Aerodyne HR-ToF-AMS. It provides a comprehensive view of the atmospheric dynamic processes responsible for the aerosol size and composition transformation. The measurements were performed at two different sampling sites (1) Indian Institute of Technology, Delhi (IITD), and (2) Manav Rachna International University, Faridabad (MRIU) during a late winter period (February to March 2018). Among organics, primary OA (POA) showed particle growth, whereas it was absent in secondary OA proxies. IITD was observed to have a distinct growth pattern as compared to MRIU because of high vehicular density and heterogeneity, and the presence of growth-promoting factors such as acidity and RH conditions. IITD aerosols were observed to be more acidic (ANR~ 0.75) compared to MRIU (ANR~1) and showed a distinct diurnal bin-wise increase during the photochemically active period (PAP). Such high acidic conditions are responsible for promoting acid-catalyzed SOA productions over the broader size bins, especially during the PAPs. Primary OA (POA) such as HOA and BBOA proxies show a diurnal growth from ~440 to 970 nm and from ~370 to 550 nm, at IITD and from ~270 to 400 nm and ~430–470 nm, at MRIU respectively. Further, OA families (amines and hydrocarbons), and inorganics such as chloride and nitrate also showed distinct concurrent diurnal growth patterns at IITD (from an MMDs of ~380–520 nm to 650–960 nm). We have also observed a positive correlation between OA and inorganics growth and the mass fraction (MF = SOA/OA) of SOA at both sites of NCR. For 0.1 (MF) increase in SOA, the sizes of HOA, chloride, primary CH family and amines (CHN family), and secondary amines (CHON family) are increased by ~93, 80, 64, 66, and 47 nm at IITD and ~14, 35, 8, 11, and 16 nm at MRIU respectively.

* Corresponding author. Department of Civil Engineering, Indian Institute of Technology, Kanpur, India.

** Corresponding author.

E-mail addresses: andre.prevot@psi.ch (A.S.H. Prevot), snt@iitk.ac.in (S.N. Tripathi).

<https://doi.org/10.1016/j.atmosenv.2021.118752>

Received 24 June 2020; Received in revised form 12 July 2021; Accepted 26 September 2021

Available online 29 September 2021

1352-2310/© 2021 Elsevier Ltd. All rights reserved.

The concurrent growth of these species with the increase in the SOA concentration indicates the existence of a similar size evolution mechanism at both NCR sites, further promoting the formation of internally mixed aerosols during some phase of their evolution. This suggests that condensation is significantly governing the growth mechanism in NCR. Our study indicates the inclusion of such dynamic growth patterns arising from local prevailing conditions into the models for a better understanding of atmospheric aerosol evolution and estimation of fine particulate matter budget.

1. Introduction

Aerosols are ‘climate changers,’ known to alter the radiative budget of the earth by indirect, direct and semi-direct effects (Albrecht, 1989; Griggs and Noguer, 2002; Jacobson, 2001). A significant mass fraction of submicron aerosol is organic Aerosols (OA) that are complex and ubiquitous in the atmosphere (Jimenez et al., 2009; Q. Zhang et al., 2007). OA can be either emitted to the atmosphere directly (primary organic aerosol, POA) or produced from the oxidation of atmospheric precursors (secondary organic aerosol, SOA). In general, SOA is more hygroscopic and less volatile than POA (Hallquist et al., 2009; Jimenez et al., 2009; Thamban et al., 2019). Condensation of SOA formation onto pre-existing POA leads to internal mixtures of POA and SOA (Jacobson, 2001), which yield morphological and chemical changes that alter the radiative forcing interactions, atmospheric aging, and cloud-nucleating ability of OA (Dusek et al., 2006; Stanier et al., 2004).

Previous studies have shown the capability of the Aerodyne high-resolution time-of-flight aerosol mass spectrometer (termed “AMS” hereafter) for real-time characterization of submicron OA in the atmosphere (Allan et al., 2003; Canagaratna et al., 2007; DeCarlo et al., 2006; Satish et al., 2017; Thamban et al., 2017, 2019; Qi Zhang et al., 2005a), including complex environments of IGP (Bhattu and Tripathi, 2015; Chakraborty et al., 2015; Thamban et al., 2017, 2019). With the AMS, size-resolved mass concentrations of non-refractory NR-PM_{2.5} (particles with less than 2.5 μm aerodynamic diameter) species can be identified in real-time (Qi Zhang et al., 2005a). Recently reported high-resolution (HR) size distribution analysis of OA proxy ions (Thamban et al., 2019) addresses the main challenge of traditional Unit Mass Resolution (UMR) size distribution studies (DeCarlo et al., 2006; Mohr et al., 2009; Qi Zhang et al., 2005b); i.e., the contributions from multiple interfering isobaric species; which can be used for the better understanding of the OA source evolution. HR analysis allows for the separation of isobaric interferences in the mass spectra and provides a more detailed view of the dynamic process by which both aerosol composition and size distribution change in the atmosphere. This comprehensive understanding will be very useful to apply in ambient aerosol models in IGP to predict the OA evolution and effect in the atmosphere accurately.

Delhi megacity, also known as National Capital Region (NCR), is a well-known aerosol hotspot located in the western Indo-Gangetic Plain (IGP) (Chowdhury et al., 2017; Gani et al., 2019; Goel et al., 2021; Kumar et al., 2016a; Lalchandani et al., 2021; Manchanda et al., 2021). NCR is a highly populated and polluted megacity in IGP that receives both local and regional aerosols from sources that include vehicular emissions, biomass burning and industrial emissions (Jain et al., 2018; Kaskaoutis et al., 2013) and these sources show strong seasonal variations (Bikkina et al., 2019). Additionally, complexities in the atmospheric evolution and mixing state of OA make its characterization more challenging (Goldstein et al., 2008; Hallquist et al., 2009) in SOA prominent environments of IGP (Kumar et al., 2016b; Thamban et al., 2019).

The aim of this study is to understand the evolution of the size and composition of fine particulate matter in the Delhi megacity during later winter. The study uses two AMSS, gas analyzers, an aethalometer, and a Single Particle Soot Photometer for the analysis. It combines the recently introduced high-resolution particle time of flight (HR-PToF) size distribution analysis with the OA factor profiles derived from the positive matrix factorization (PMF). The present study is performed during the

late winter season (February to March 2018) at two NCR sites.

2. Methods

2.1. Sampling locations

The sampling sites were: the Centre for Atmospheric Sciences building (28.547° N 77.191°E, 242 m above mean sea level) in the Indian Institute of Technology-Delhi campus (IITD) and the Faculty of Engineering and Technology block of Manav Rachna International University (MRIU) (28.450°N, 77.283°E, 253 m above mean sea level). IITD is located in south Delhi, observed to have a high RH during the winter period and has influence from vehicular emissions from an arterial road (Gani et al., 2019) that located ~100 m away from the sampling location. MRIU is situated in Faridabad, a known industrial hub that is located in the south-west of the NCR and influenced by the traffic emissions from a bypass road located ~100 m north-east of the sampling site. The instruments were housed in temperature-controlled laboratories at both sampling locations. MRIU is located in the downwind direction of IITD, and the aerial distance between the sampling locations is ~20 km (Lalchandani et al., 2021; Wang et al., 2020). The sampling sites location and their areal distances adapted from google maps are shown in Fig. S1a.

The study periods were a late winter period, i.e., February 7, 2018 to March 10, 2018 at IITD and 2nd February to March 15, 2018 at MRIU. During the sampling period, both sites experienced lower temperatures (~20 °C; Fig. S1b) and varying Relative humidity (RH~34–100% at IITD and ~15–90% at MRIU; Fig. S1b), and shallow boundary layer height which promotes the accumulation of pollutants at ground level.

To understand the influence of climatology at Delhi megacity on the downwind sites, we have performed HYSPLIT forward frequency analysis (Draxler et al., 2016; Stein et al., 2015) at MRIU between 1st February to March 8, 2018. The total forward trajectory duration was five days, and new trajectories are calculated for every 12 h for a height of 500 m above ground level with a 1° × 1° resolution. Forward HYSPLIT frequency analysis indicates that the aerosol composition at the sampling sites significantly influences local and regional downwind receptor sites climatology (Fig. S9).

2.2. Instrumentation

At each site, the real-time size distribution and chemical composition of the non-refractory aerosol species were measured using Aerodyne HR-ToF-AMS (AMS). At IITD and MRIU, aerosols were sampled through PM_{2.5} and PM₁ lenses, respectively. The higher lens diameter at IITD increases its collection efficiency and significantly extend the transmission efficiency towards the big diameter particles (as PM_{2.5} lens successfully transmits more than 50% of PM_{2.5}) (Williams et al., 2013), while the PM₁ lens at MRIU has a 100% transmission efficiency for a smaller size range, i.e., from 70 nm to 600 nm (Allan et al., 2003). The duty cycle of the chopper and the PToF length of AMS at each NCR sites were 2% and 0.295 m.

With the AMS, non-refractory species were quantified by the electron ionization (70 eV) of the thermally vaporized (~600 °C) aerosols (Canagaratna et al., 2007). The AMS operating mode is switched between particle time of flight (PToF) mode and mass spectrum (MS) mode with a time resolution of 2 min at both the sites. The sampled aerosols

were dried using an aerosol sample dryer system (Aerodyne research, Inc) at IITD and using a silica diffusion dryer regenerated frequently at MRIU to achieve the output RH \sim 20%. The regression analysis (Fig. S16) shows that the slopes (indicate the $\text{NH}_4/\text{NH}_4^{\text{predicted}}$) of 0.7 for IITD and 0.99 MRIU, representing that the aerosols are not that acidic to changes the collection efficiency from 0.5 at both the sampling site. The ammonium nitrate mass fractions (ANMF) were calculated for both the sites, which were less than 0.4. Therefore, none of these effects were substantial to change collection efficiency (CE) from the default value of 0.5. More details of the CE can be found in (Lalchandani et al., 2021; Middlebrook et al., 2012). The ionization efficiency (IE) calibrations were done once before the sampling period at MRIU and IITD. The calculated relative ionization efficiency (RIE) values for NH_4^+ were 3.89 and 4.1, respectively, for IITD and MRIU. Organics, Cl^- and SO_4^{2-} were assumed to have RIE values that were 1.4, 1.3, and 1.2, respectively, at each site of NCR (Canagaratna et al., 2007). The vacuum aerodynamic diameters (D_{va}) of the non-refractory aerosols are derived from the particle velocities in AMS (Canagaratna et al., 2007; DeCarlo et al., 2004). The size calibrations of AMS were performed with ammonium nitrate at each sampling site with NH_4NO_3 . The size calibration comparison for IITD and MRIU is shown in Fig. S5.

Seven wavelengths Aethalometer (AE-33), manufactured by Magee Scientific, USA (Drinovec et al., 2015), and Single Particle Soot Photometer (SP2), manufactured by Droplet Measurement Technologies (DMT) (Moteki and Kondo, 2007, 2010, 2007; Schwarz et al., 2006; Stephens et al., 2003) were used to measure the black carbon (BC) concentrations at IITD and MRIU respectively. Trace gases including oxides of nitrogen (NO_x , i.e., $\text{NO} + \text{NO}_2$) and carbon monoxide (CO) were continuously measured at IITD and MRIU using the Serinus gas analyzers (model number: serinus 40 and 30 respectively) that manufactured by Ecotech, Australia, and Thermo Scientific monitors (model 42i and 48i respectively) that manufactured by Thermo Scientific, USA. Ozone was additionally measured at MRIU (model number: 49i) using the gas analyzer manufactured by Thermo Scientific, USA. During the sampling period, volatile organic compounds (VOCs) also were quantified with two proton-transfer-reaction time-of-flight mass spectrometers (PTR-ToF-MS) at the same sampling sites (Wang et al., 2020).

2.3. Data analysis

The unit mass resolution (UMR) and high resolution (HR) data analysis were performed (Canagaratna et al., 2007) on the AMS data for both sites using SQUIRREL (Version 1.62) and PIKA (Version 1.22). High-resolution (HR) peak fittings were performed on the AMS-derived mass spectra (MS) using PIKA (DeCarlo et al., 2006), and is further processed to identify the size-resolved mass spectra of HR species. The HR-PToF size distribution is estimated using the same PIKA (Version 1.22). The size distributions were derived from the PToF mode measurements that are normalized to the UMR MS data. Two direct current (DC) regions, where the particle velocity is too low or high to be transmitted in AMS, were identified to remove the baseline ion signals. DC regions were selected at a smaller (DC region-1) and a higher (DC region-2) PToF times, to separate the overlapping contribution of the signal from interfering particle and gas fragments such as ammonium aerosol at m/z 15, $^{15}\text{N}^+$ from the air (Allan et al., 2003) and also gas-phase CO_2^+ fragment at m/z 44. DC1 regions of MRIU ($D_{\text{va}} = 30$ nm–47 nm) and IITD ($D_{\text{va}} = 12$ nm–42 nm) was selected as the background signal to subtract the gaseous fragment interferences. A composition-dependent collection efficiency (CDCE) of 0.5 was applied to the mass concentrations of all species derived from AMS as described elsewhere at each site (Middlebrook et al., 2012). Methods described originally by (Aiken et al., 2008) and updated by (Canagaratna et al., 2015) were used to find the elemental ratios from the high-resolution mass spectra of AMS at each site.

To understand the sources of OA at MRIU and IITD, Positive matrix factorization (PMF) (Paatero and Tapper, 1994) was performed by

(Lalchandani et al., 2021) on the HR V-mode, 2 min averaged organics data at each site using Source Finder (SoFi) interface that works through the multilinear engine (ME-2) (Bozzetti et al., 2016; Canonaco et al., 2013). The PMF factors were identified based on physical interpretability, correlation with internal and external markers, and scaled residuals (Ulbrich et al., 2009).

2.3.1. Estimation of HR-PToF size distribution

For simplicity, the size-resolved analysis of high-resolution AMS mass spectra is referred to as HR-PToF analysis in this manuscript (Thamban et al., 2019). To speed up the data process, and increase the signal to noise ratio for HR fitting, the raw data (2 min alternatively for each mode: PToF and MS) was averaged to 3 h. In HR-PToF analysis, the peak fitting parameters such as HR peak width, and m/z calibration and HR peak shape of MS data were assumed to be the same for the HR-PToF data. Detailed procedures for HR-PToF analysis are explained in (Thamban et al., 2019).

Particle Time of flight (PToF) size data were grouped into thirteen equally-spaced PToF bins ($\Delta t = 0.00033$ s) with diameters ranging from 0 to 2582 nm at MRIU (Table S2). At IITD, The data was grouped into fifteen bins (thirteen equally spaced PToF with $\Delta t = 0.00024$ s (diameter range = 5–1684 nm) and two equal PToF bins with slightly higher Δt values of 0.0003 s (diameter range = 1684–2851 nm)) (Table S1). Each PToF bins at both the sites have exponentially increasing vacuum aerodynamic diameter (D_{va}) values with PToF time. The mean bin diameter (MBD) indicate the geometric mean of D_{va} values of a particular HR-PToF size bin. Mean Modal diameters (MMD) represent the mean of the HR size distribution modes at a particular period of a day. The details of MMD are described in (Thamban et al., 2019). The appropriateness of using MMD to characterize the particle growth is illustrated in Fig. S12, which shows the difference in the particle size is well-captured by representing them with MMD.

3. Results and discussion

3.1. HR size distributions of OA proxies

OA source apportionment is performed using a positive matrix factorization (PMF), which works on the advanced multi-linear engine (ME-2) model. High mass-resolved OA mass spectra at IITD and MRIU are factorized into six sources that include a low volatile oxygenated OA (LVOOA), two semi-volatile oxygenated OAs (SVOOAs), two solid-fuel combustions OAs (SFC-OAs), and a hydrocarbon like OA (HOA) at each sampling site. Oxygenated OA (sum of LVOOA and SVOOAs) contributes the predominant fraction of OA mass (52–55%) with maximum afternoon hours contribution. HOA contributes 9–20%, and SFCs contribute 27–36% at the two sites of NCR. The average percent contributions of PMF derived OA factors to the total mass of OA at IITD and MRIU are shown in Fig. S1c. The mass spectra of OA factors identified at the IITD and MRIU sites are shown in the S13. More details of the PMF factors selection, diagnostics, and interpretation can be found in the companion manuscript (Lalchandani et al., 2021).

OA source apportionment studies have identified several proxies such as m/z 43 for SVOOA (Decarlo et al., 2010), m/z 44 for LVOOA (m/z 44) (Q. Zhang et al., 2005), m/z 60 and m/z 73 for BBOA (m/z 60 and m/z 73) (Aiken et al., 2008; Jimenez et al., 2009), m/z 57 for HOA (m/z 57) (Mohr et al., 2009) using UMR-AMS data. Understanding the size distributions of HR isobaric ions fitted at these OA proxies (m/z 43, m/z 44, m/z 57 and m/z 60) are very important to address the evolution of size-resolved chemical compositions of OA in unique environments like NCR where the aerosols are complex in origin and atmospheric processing.

Figs. 1 and 2 show the size distributions of these UMR proxies at IITD and MRIU and illustrate the extent to which these size distributions are influenced by the constituting size distributions of the isobaric HR fragments that can be of different origin and atmospheric age. HR size

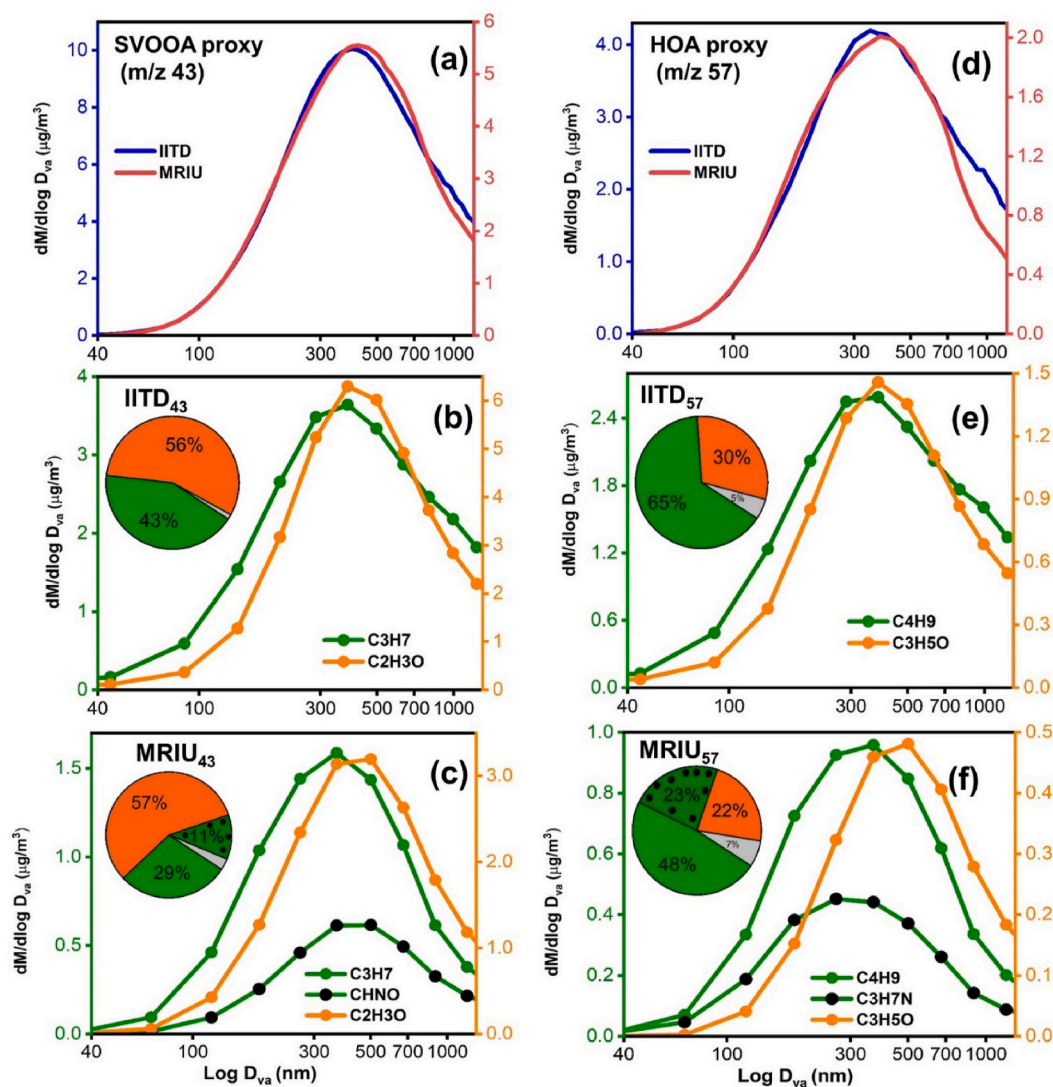


Fig. 1. UMR size distributions of (a) SVOOA (m/z 43) and (d) HOA (m/z 57) proxies at IITD and MRIU. Fig. 1b and c represent the HR size distribution at SVOOA proxies at IITD and MRIU, respectively Fig. 1e and f represent the HR size distribution at HOA proxies. The Y-axis mass concentrations are normalized to corresponding HR MS fragments. Pie charts at 1b,c,e,f are indicating the fractional contributions from primary and secondary fragments towards the mean mass of UMR proxy.

distributions at IITD and MRIU have fewer data points (15 and 13, respectively) than the corresponding UMR distributions (61 and 78 respectively) as they are calculated by averaging over the wider size bins. The mass contribution of individual isobaric HR fragments towards the mean mass of the respective UMR OA proxy is termed as its fractional contribution (f_x) in the further discussion of this manuscript. Pie charts in the second and third rows of Figs. 1 and 2 indicate the f_x of HR ions towards the mean mass of UMR proxies at these sites. f_x along with its standard deviation is used in the further discussion of this section.

The UMR size distributions of SVOOA (m/z 43) and HOA (m/z 57) proxies and the size distributions of the contributing HR fragments at these m/z 's at IITD and MRIU are shown in Fig. 1a–f. At IITD, SVOOA proxy has contributions from primary ($C_3H_7^+$) and secondary ($C_2H_3O^+$) organic fragments that have an f_x of 43 ± 13 and $56 \pm 11\%$, whereas, at MRIU, they contribute 29 ± 8 and $57 \pm 7\%$, respectively. A notable fraction of secondary organo-nitrate ($CHNO^+$) fragment is also seen with an f_x of $11 \pm 2\%$ at MRIU (Fig. S2).

The modal diameter of the SVOOA proxy (m/z 43) at MRIU is slightly higher (420 ± 11 nm) than that of IITD (398 ± 13 nm) (Fig. 1a). The details of UMR-PTOF bin edges, geometric mean bin diameters, and the bin widths at IITD and MRIU are shown in the supplementary section as

Table S3. The diameters are round to the nearest whole number in the discussions. At MRIU, size distributions of constituting primary ($C_3H_7^+$) and secondary fragments ($C_2H_3O^+$ and $CHNO^+$) show distinct modes at 368 and 501 nm, respectively (Fig. 1c). These different modes are absent at IITD (Fig. 1b), where both the primary ($C_3H_7^+$) and secondary $C_2H_3O^+$ fragments have the same size distribution modes at 384 nm. $C_3H_7^+$ is a POA fragment generally emitted from engine exhaust, plastic burning, and meat cooking (Mohr et al., 2009). Conversely, $C_2H_3O^+$ is a principal secondary oxygenated organic fragment in atmospheric OOA (Ng et al., 2010).

The size distribution of the UMR HOA proxy (m/z 57) is shown in Fig. 1d. The mode of the size distribution of individual species is indicated further as ‘mode’ in this manuscript. HOA proxy (m/z 57) at MRIU shows a higher mode of (379 ± 10 nm) compared to that of IITD (347 ± 12 nm). At IITD, m/z 57 is composed of a primary hydrocarbon ($C_4H_9^+$) and a secondary oxygenated ($C_3H_5O^+$) fragment (Fig. 1e) with an f_x of $65 \pm 10\%$ and $30 \pm 9\%$ respectively, and the modes of primary ($C_4H_9^+$) and secondary ($C_3H_5O^+$) fragments that are located at a diameter of 384 nm, with an increased concentration of primary isobaric $C_4H_9^+$ fragments at lower diameters. At MRIU, in addition to these $C_4H_9^+$ ($f_x = 48 \pm 6\%$) and $C_3H_5O^+$ ($f_x = 22 \pm 6\%$) fragments, a primary organo-nitrate

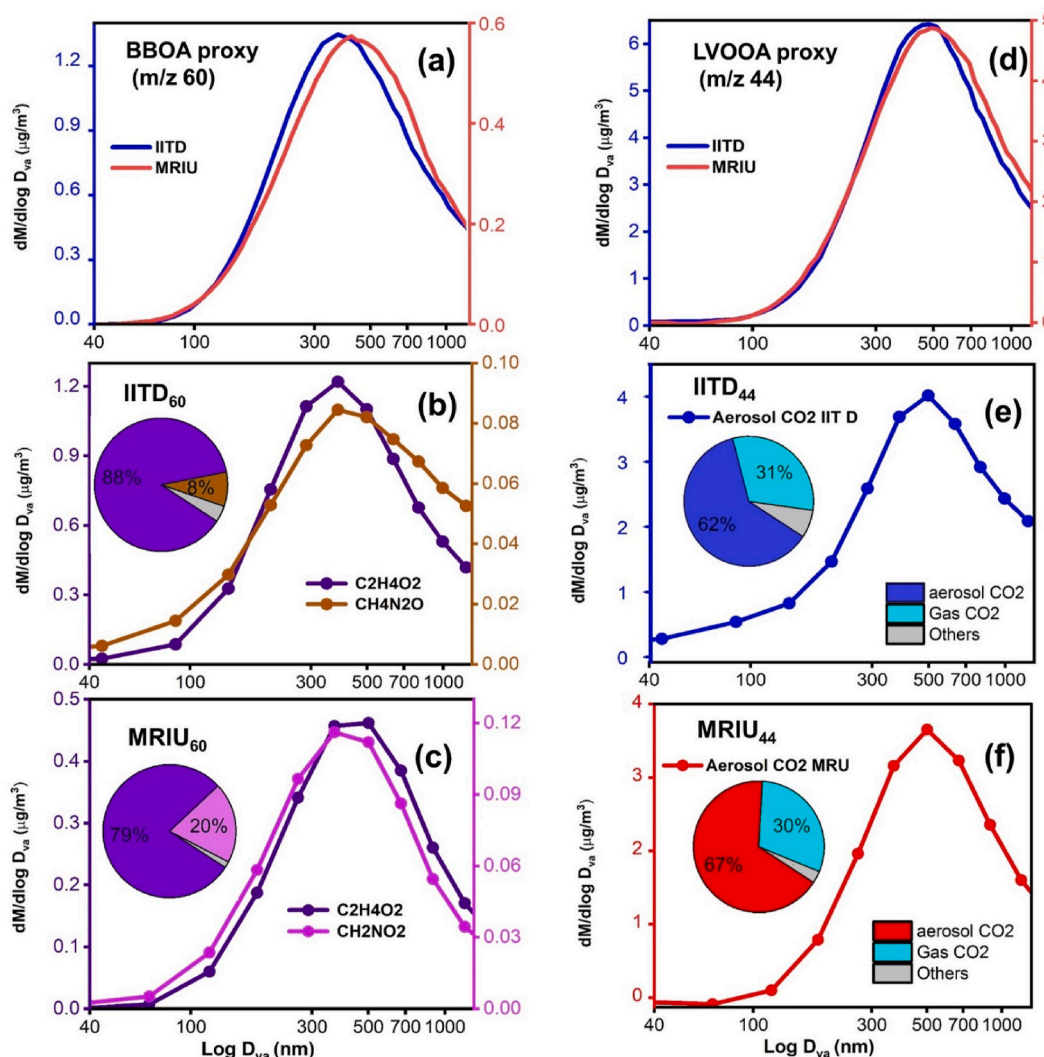


Fig. 2. The UMR size distribution of BBOA (a) and LVOOA (d) proxies. Fig. 2b and c represent the HR size distribution at BBOA proxies at IITD and MRIU, respectively. Fig. 2e and f represent the HR size distribution at LVOOA proxies at IITD and MRIU, respectively. Y-axis is scaled from PToF to MS. Pie charts at 2b,c,e, and f are indicating the fractional contributions from primary and secondary fragments towards the average mass of respective proxies.

fragment, i.e., $C_3H_7N^+$ ($f_x = 23 \pm 5\%$) is also contributing (Fig. S3a) towards the mean mass of HOA proxy (Fig. 1f). Primary $C_3H_7N^+$ fragment shows the broader peaking at lower diameters, i.e., 264–368 nm, non-oxygenated ($C_4H_9^+$), and oxygenated ($C_3H_5O^+$) fragments show distinct peaks at 368 nm and 501 nm at MRIU.

It is interesting to note the size distributions of $C_4H_9^+$ at IITD and MRIU with previous studies. IITD and MRIU are observed to have size distributions of $C_4H_9^+$ that peak at D_{va} 384 and 368 nm, respectively, and are higher than the sizes of HOA proxies measured in the other ambient environments (Aiken et al., 2008; Alfarrar et al., 2007), vehicular exhaust (Canagaratna et al., 2004), and water pump engine exhausts (Douglas Goetz et al., 2018), i.e., $D_{va} \sim 100$ nm (Canagaratna et al., 2004; Douglas Goetz et al., 2018; Qi Zhang et al., 2005b). However, the similar sizes of the $C_4H_9^+$ at NCR sites (D_{va} of 384 and 368 nm) and Kanpur ($D_{va} \sim 350$ nm) (Thamban et al., 2019) could be indicating that 1) similar HOA sources in these sites of IGP 2) rapid growth of HOA due to the condensation of SOA than the other sites 3) possible atmospheric processing of some fraction of freshly emitted HOA in NCR sites. HOA particles with $D_{va} < 70$ nm could not detect well using AMS, hence not discussing in the current manuscript.

To understand more details of the $C_4H_9^+$ distributions, it is important to understand its interaction with mass fractions of HOA and SFC

factors. The mass fraction of each OA source is termed as its 'MF' hereafter in this manuscript. The ratio of MF of HOA to the total SFC (SFC1+SFC2) is indicated as HOA/SFC. At MRIU, HOA/SFC increases (Fig. S8a) with the increase in the diameter of $C_4H_9^+$, contrarily, while in the case of IITD, it decreases (Fig. S8b). The prominent size of HOA during high SFCs periods could be indicating the condensation derived growth of HOA at these periods at IITD. On the contrary, on the high SFC period, MRIU shows low diameters, which could be due to the difference in atmosphere processing and sources of SFCs at these sites.

Fig. 2 shows the UMR size distributions of BBOA (m/z 60) and LVOOA (m/z 44) proxies and the size distributions of constituting HR OA fragments fitted at these UMR proxies at IITD and MRIU. The mode of size distributions of m/z 60 (Fig. 2a) at MRIU (420 ± 11 nm) is higher than that of IITD (372 ± 13 nm). However, in the case of m/z 44 (Fig. 2d), both sites have close modes, i.e., 484 ± 15 nm at IITD and 489 ± 12 nm MRIU, respectively. BBOA is generally characterized by the distinct fragments of levoglucosan, i.e., $C_2H_4O_2^+$ and $C_3H_5O_2^+$ at m/z 60 and 73, respectively. We have only discussed the size distribution of the $C_2H_4O_2^+$ fragment further in this manuscript. The size distributions of $C_3H_5O_2^+$ do not show much difference with $C_2H_4O_2^+$ and its relative concentration is less than $C_2H_4O_2^+$ (Fig. S15). The UMR BBOA proxy (m/z 60) at IITD and MRIU shows predominant contributions from

$C_2H_4O_2^+$ fragments ($f_x = 88 \pm 4$ and $79 \pm 3\%$ respectively) and show influences from oxygenated organo-nitrate fragments such as $CH_4N_2O^+$ ($f_x = 8 \pm 2\%$) and $CH_2NO_2^+$ ($f_x = 20 \pm 4\%$) respectively in its HR peak fitting (Fig. S4). The higher f_x of $CH_2NO_2^+$ and its modal differences with $C_2H_4O_2^+$ at MRIU makes the size distribution of m/z 60 more complex there than IITD.

CO_2^+ is a well-known proxy and principal contributing fragment of highly aged Low volatile oxygenated OA (LVOOA). The mode of the HR size distributions of aerosol CO_2^+ is at a D_{va} of 498 and 501 nm for IITD (Fig. 2e) and MRIU (Fig. 2f), respectively, and consistent with the UMR LVOOA proxy (m/z 44) distributions at these sites (mode 484 ± 15 nm for IITD and 489 ± 12 nm for MRIU). Fig. 2c and f indicate that the UMR LVOOA proxy (m/z 44) size distribution measurements can be prone to interference up to $\sim 30\%$ due to gaseous CO_2^+ detected in the PToF mode of AMS. However, the interferences of gaseous CO_2^+ are not causing a notable change in the UMR size distributions (compared to HR) in the present study, hence not discussing in detail.

In NCR, fragments of hydrocarbons have relatively higher mass contributions from lower diameters than that of oxygenated fragments. This pattern of hydrocarbon and oxygenated fragments is consistent with the previous study at another highly polluted site in IGP (Thamban

et al., 2019) and agree with the previous studies by (Mohr et al., 2012; Q. Zhang et al., 2005) that indicated the smaller diameter peaks for the distributions of UMR proxies of primary OA, i.e., COA and HOA than oxygen containing secondary OOA proxies.

Altogether, the mode of the distribution of UMR proxies and the constituting HR fragments at MRIU is slightly higher than that of IITD. It is interesting to note that the difference in the modes of the distribution between primary and secondary fragments is more distinct at MRIU than IITD. One of the possibilities of this difference in the modes of average distribution between MRIU and IITD can be correlated with the freshly emitted OA near the vicinity of IITD, and being a downwind site, MRIU receives OA that undergone more atmospheric processing that, in turn, can increase its size. However, to understand the size and growth of primary and secondary fragments, more careful, detailed examinations are required, which is discussed in sections 3.2 to 3.5. “~” is used in the following sections of this manuscript to indicate the diameters in a whole number and to increase its readability.

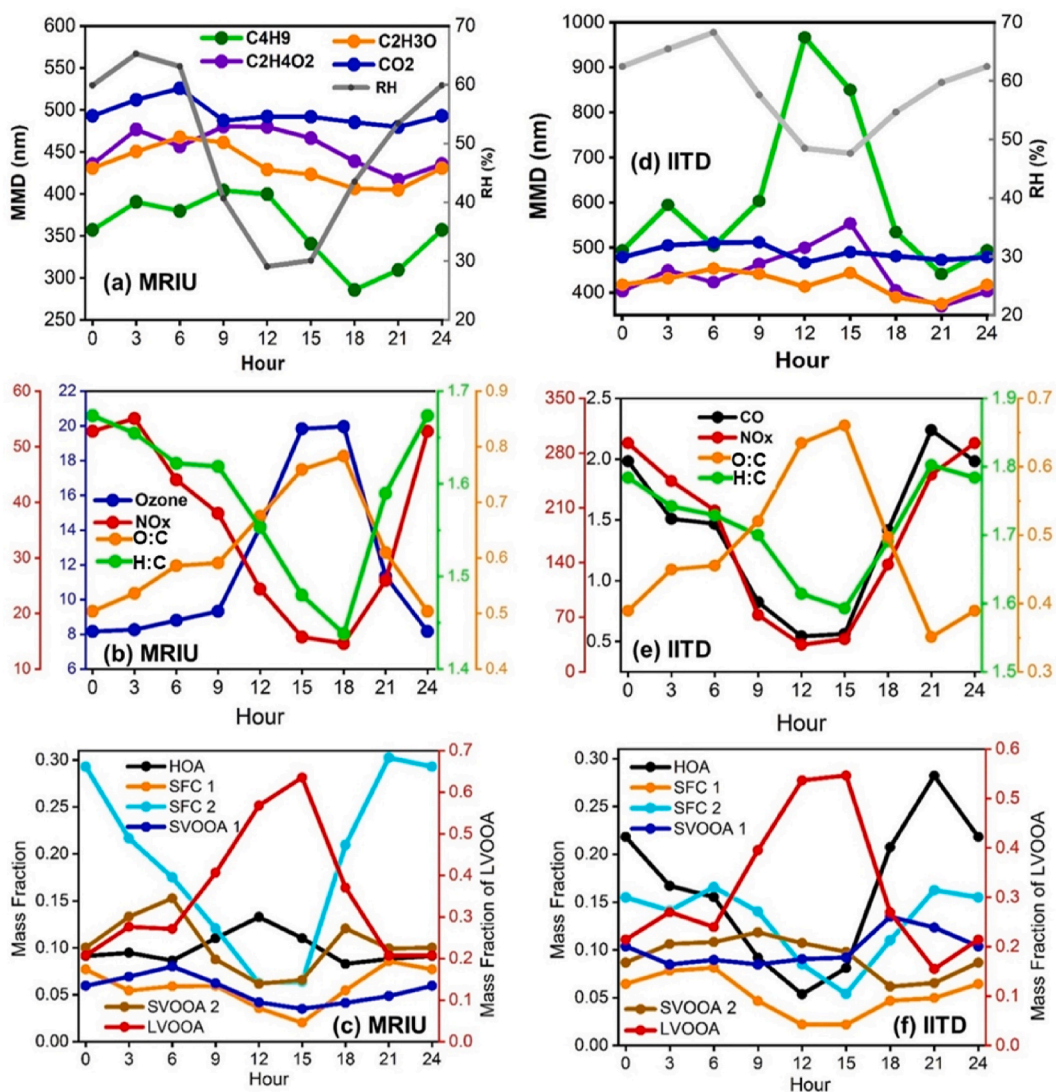


Fig. 3. The diurnal variation of 3-h averaged Mean Modal Diameters (MMDs) of HR species and relative humidity (RH) at (a) MRIU and (d) IITD. Fig. 3b and e represent the diurnal variation in the O/C, H/C ratio derived from AMS, and the gaseous concentrations at MRIU and IITD, respectively. The gaseous concentration of NO_x and Ozone are shown in ppb, and CO is shown in ppm in the y-axis of Fig. 3b and e. Fig. 3c and f indicate the diurnal mass fractions of PMF derived factors.

3.2. Diurnal trends of mass concentration and MMD of HR organic proxies

Fig. 3 shows 3-h averaged diurnal variations of MMDs of HR ion proxies for HOA ($C_4H_9^+$), BBOA ($C_2H_4O_2^+$), SVOOA ($C_2H_3O^+$) and LVOOA (CO_2^+), their relationship with the relative humidity (RH), elemental ratios, trace gas concentrations and PMF derived OA sources at IITD and MRIU.

Both sampling sites have predominant MF of LVOOA that contribute up to ~50–60% during the photochemically active periods (Fig. 3c, f). Previously (Aiken et al., 2008) has reported the daytime production of OOA species in urban environments. This increase in the mass fractions of LVOOA along with the increase in O/C ratio at both the sites indicates the production of SOA due to local photochemistry or influx of regional OA during boundary layer expansion at the daytime (Lalchandani et al., 2021; Wang et al., 2020). This daytime SOA production can be correlated with the increased daytime concentration of ozone (Fig. 3b) that produced due to photochemical reactions (Gaur et al., 2014; Holt, 1961). The simultaneous increase of the O/C and MF of LVOOA indicate the SOA formation and atmospheric aging can be the key mechanism that determines the growth of POA at both sites.

Fig. 3b and c and 3e-f show the diurnal variations of 3-h averaged trace gas concentrations, elemental ratios, RH, and PMF derived mass fractions of OA sources at two sites. Primary biomass burning proxy ($C_2H_4O_2^+$) (Aiken et al., 2008) shows the daytime growth from MMD of ~370 (21:00 LT) to ~550 nm (15:00 LT) at IITD. However, this notable growth pattern is absent at MRIU, where the MMD of $C_2H_4O_2^+$ has only increased from ~430 (21:00 LT) to ~470 nm (noon). Secondary fragments such as $C_2H_3O^+$ and CO_2^+ do not show any visible diurnal pattern at MRIU and IITD.

At both sites, $C_4H_9^+$ shows the lowest MMDs at peak emission periods (18:00–21:00 LT). Peak emission periods increase the fresh, externally mixed HOA number concentration from cars and motorbikes (and due to decreased boundary layer heights). These freshly generated HOA doesn't have enough time to grow due to condensation or coagulation and can result in low MMDs. The MMDs can also be affected by the operating velocity of vehicles at this peak traffic load period (Yang et al., 2005). found that Asian four-stroke motorcycle emissions have a bimodal distribution with mode below and above D_{va} of ~100 nm and the size distributions of motorcycle emissions shifted to lower diameters when they were operating 15–30 km/h (Chien and Huang, 2010) and even up to ultrafine ranges when vehicles are operated above idle (Douglas Goetz et al., 2018). Similar patterns of low MMDs of $C_4H_9^+$ are seen at peak emission periods (18:00–21:00 LT) at both the sites. This peak emission periods are characterized by the increase in the number concentration of BC aerosols (Fig. S14a), increase in NO_x concentrations, and increase in HOA concentrations (Fig. S1d). The shifting of $C_4H_9^+$ towards lower diameters can also results from the lower operating velocity of vehicles (due to the increased traffic congestion due to peak period near the sampling sites) and the decrease in boundary layer heights at these sites.

During daytime (6:00 LT–18:00 LT), $C_4H_9^+$ grows significantly to higher diameters such as ~950 nm at noon and ~850 nm at 15:00 LT (Fig. 3d) at IITD. This distinct growth pattern around 12:00–15:00 LT is absent at MRIU (Fig. 3a) and shows a relatively constant MMD ~410 nm till noon of the day that decreases to the minimum MMD at the peak emission period. Size distributions (Fig. S6b) at the lowest HOA concentration period (15:00 LT, Fig. S6a) at both sites indicating that the size distributions are not affected by low concentration artifacts.

Higher MF of HOA (~2.5 fold) and concentrations of NO_x (~6 fold) at IITD than MRIU indicating that the increased MF of HOA at IITD is dominantly contributed from the internal combustion engines (Lanz et al., 2007) at the vicinity of IITD at nighttime (Fig. 3b,e). However, during the daytime, HOA MF showed contrasting diurnal patterns that increased to a maximum value of ~0.13 around noon at MRIU and correspondingly decreased to a minimum MF of ~0.05 at IITD that could

result from the steep decrease in MF of SFC2 factor and the additional fresh vehicular emissions from the MRIU campus. The hourly diurnal variation in the mass concentration of HOA and NO_x (in ppb) at IITD and MRIU are shown in the supplementary information S1d. Fig. S1d shows that a small morning rush hour peak between 08:00–09:00 LT and a sharp peak between 18:00–23:00 LT at both the sites for HOA and NO_x . High HOA concentration at night-time could result from the lower boundary layer and night-time emission from the heavy-duty vehicles that are only allowed to enter the Delhi megacity during night-time, which is extensively discussed in the companion manuscript (Lalchandani et al., 2021).

Similar to HOA proxy, primary BBOA proxy ($C_2H_4O_2^+$) is also not shown the daytime growth at MRIU, which could be due to the difference in source contribution, lens difference, and atmospheric interactions compared to IITD where $C_2H_4O_2^+$ is grown from ~396 to 553 nm. The $PM_{2.5}$ lens used at IITD has an extended transmission efficiency towards 2.5 μm and transmits more than 50% of $PM_{2.5}$ (Williams et al., 2013) while, the PM_1 lens at MRIU has a relatively narrower transmission efficiency range (from 70 to 600 nm) (Allan et al., 2003). These differences in the lenses will result in underestimating OA's growth above 600 nm at MRIU.

As discussed in earlier, it shows from Fig. S8 that the BBOA sources (SFCs) are interfering with the size of the HOA at both the sites in contrasting way and depends much on the sources and atmospheric processing of SFCs at these sites.

To understand the possible origin and travel path OA sources, back-trajectory analysis is performed using the HYSPLIT model (v4.1, Hybrid Single-Particle Lagrangian Integrated Trajectory) (Draxler et al., 2016; Stein et al., 2015) using Global Data assimilation system (GDAS) files with $1^\circ \times 1^\circ$ resolution. The back trajectories were weighted with OA sources (derived from PMF) using a concentration weighted trajectory (CWT) model to confine the air parcels accountable for high aerosol concentrations at the receptor sites. The detailed analysis and methodology of CWT analysis can be found in Lalchandani et al., 2021. CWT-derived plots are shown in Fig. S10.

CWT plots indicate that HOA is originated locally for IITD and MRIU. SFC-1 at both the sites are influenced by the transported air masses from the north-west direction and close to the sampling location. Local sources contribute to the high SFC-2 concentration at both the sampling site. For SVOOA-1, the probable source of high concentration was local emissions and the emissions from the north-west direction. SVOOA-2, on the other hand, is probably originated from the south-east direction and local in origin at IITD, whereas it appears to be originated from the local sources and north-west direction at MRIU. LVOOA appears to be originated from the south-east direction and at the proximity of the sampling site at IITD, whereas at MRIU, it probably originates from the emission from close vicinity and north-west direction. The details of CWT-derived interpretations can be found in the companion paper (Lalchandani et al., 2021).

3.3. Diurnal trends of MMDs of HR-OA families, inorganics and $C_4H_9^+$

Along with the OA proxies, it is important to understand the diurnal variations of the MMDs of OA families and inorganic species. Fig. 4a–h indicates the diurnal variation in the MMDs of OA families, inorganics, and the mass concentrations of amines at MRIU and IITD. At both sites, the CH family show distinct diurnal growth pattern (4a and 4e) than CHO and CHOgt1 families. The growth of CH family at IITD is more prominent (from ~380 (21:00 LT) to ~760 nm (15:00 LT)) than that of MRIU (from ~370 (21:00 LT) to ~465 nm (6:00 LT)). Similarly, more distinct growth for the CHO family is observed at IITD (from ~400 (21:00 LT) to ~525 nm (15:00 LT)) than that of MRIU (from ~400 (21:00 LT) to ~480 nm (06:00 LT)). CHOgt1 family shows a lesser growth than CH and CHO family at both sites. Along with these CH and CHO families, it is interesting to see the growth of amine families (CHN and CHON families) at both sites. CHN family grows from ~521 (21:00

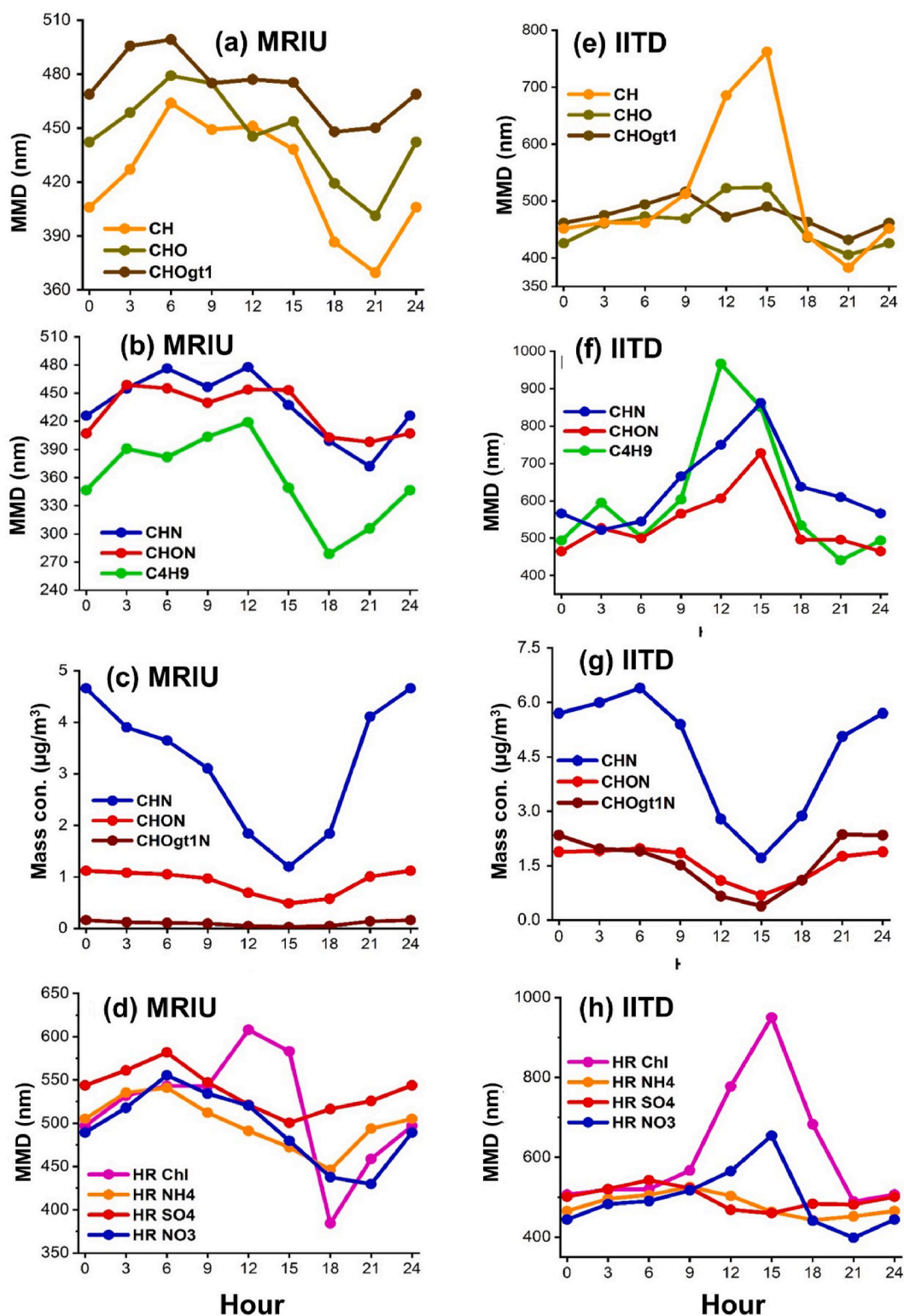


Fig. 4. Diurnal variations of MMDs of various organic families, $C_4H_9^+$, inorganics (anions and cation), and the mass concentrations of organo-nitrate families at MRIU and IITD. The diurnal MMDs variations of organic families, $C_4H_9^+$, and inorganics at MRIU (a,b, and e respectively) and IITD (e,f, and h respectively). 4(c) and (g) indicates the 3-h averaged mass concentration of organo-nitrates at MRIU and IITD, respectively.

LT) to ~ 860 nm (15:00 LT) at IITD and from ~ 370 (21:00 LT) to ~ 480 nm (noon) at MRIU. Similarly, at IITD, CHON shows a prominent growth from ~ 464 (midnight) to ~ 730 nm (15:00 LT) at IITD and a lesser distinct growth from ~ 400 (midnight) to ~ 455 nm (noon) at MRIU.

Fig. 4d and h indicate the diurnal MMD variation of inorganic anions

and cation for MRIU and IITD, respectively. In the case of inorganics, chloride has shown a prominent growth at IITD (Fig. 4h) (from ~ 490 (21:00 LT) to ~ 950 nm (15:00 LT)) than that of MRIU (~ 380 (18:00 LT) to ~ 610 nm (12:00 LT)) (Fig. 4d). Nitrate (NO_3^-), an SVOOA proxy, also shows a notable growth from ~ 400 to ~ 650 nm at IITD (Fig. 4h) than

that of MRIU, i.e., ~ 430 (21:00 LT) to ~ 550 nm (Fig. 4d). Other secondary inorganics such as NH_4^+ and SO_4^{2-} do not show observable growth at both sites. It is interesting to see the growth of primary emitting chloride, similar to that of C_4H_9^+ at both the sites. The semi-volatile nitrate (NO_3^-) fragments also show growth from ~ 420 to 550 nm and ~ 400 – 650 nm at MRIU and IITD, respectively. Regionally transported sulfate (SO_4^{2-}) shows the least variation of MMD at both sites. We speculate a significant fraction of ammonium (NH_4^+) can be regionally transported as it shows least variation of MMD at both sites.

It is seen that the diurnal growth pattern of HOA (C_4H_9^+) is correlated well with the growth pattern of the families of hydrocarbon (CH family, Fig. 4a and e), primary and secondary amines (CHN and CHON families, Fig. 4b and f) and inorganic chloride (Fig. 4d and h) at both sites. As seen in earlier discussions, the growth of HOA with OA families and inorganics are less prominent at MRIU, especially at PAP due to the previously discussed reasons. The similar diurnality of MMDs of CH family and HOA at both sites indicate that all the hydrocarbon fragments show a similar growth pattern despite their complex sources. The concurrent increase in the MMDs of the families of CH, amines (CHN, CHON), chloride, and HOA indicates that species are internally mixed at both sites in NCR during their atmospheric evolution.

Additionally, the sizes of OA proxies and families are compared with the ambient temperature to understand their interactions. At IITD, it is found that the sizes of HOA and OA families are positively correlated with the temperature. However, such a positive correlation is not seen at MRIU (Fig. S11). As the SOA formation can primarily cause these growths at IITD at noon period (which is also characterized by high ambient temperature), the sole effects of temperature on OA and families size cannot be determined in the present manuscript. Additionally, the temperature at which 50% of the mass remains for a given OA component (T_{50}) is generally high for OA (Cappa and Jimenez, 2010), identified at T_{50} value range from ~ 100 °C to ~ 225 °C for volatile components of OA. Another study (Huffman et al., 2009) identified the average T_{50} of 102 – 107 °C for OA, 133 – 154 °C for LVOOA, 85 – 94 °C for HOA, 87 – 92 °C for SVOOA. As these temperatures are well above the sampling temperature, a consistent correlation between the size and temperature cannot be achieved at the sampling sites.

3.4. Size resolved aerosol neutralization ratio (ANR)

Aerosol neutralization ratios (ANRs) that represent the normalized molar ratio of NH_4^+ concentration measured to the NH_4^+ concentration needed for the complete neutralization of anions are calculated at IITD and MRIU to identify the degree of stoichiometric neutralization of measured aerosols (Chakraborty et al., 2015; Thamban et al., 2019; Qi Zhang et al., 2007). This ANR indicates the extent of the acidity of aerosols (Qi Zhang et al., 2005a). Acidic atmospheric aerosols are more hygroscopic than their neutralized forms and show a positive correlation with the atmospheric water content (Qi Zhang et al., 2007). It is important to note that the analysis performed in this section is based on the ion ratios, which are not a direct measure of aerosol acidity.

Size-resolved mass concentrations of ammonium (NH_4^+), nitrate (NO_3^-), sulfate (SO_4^{2-}), and chloride (Cl^-) are calculated from the HR-PTof analysis, that further scaled to PIKA fitted MS mode mass concentrations of these inorganic species. ANRs are calculated by assuming that the only cation that neutralizes the anions is NH_4^+ (Chakraborty et al., 2015), which is formed from the gas phase ammonia (NH_3) that is generated during agricultural activities (Weber et al., 2016) and gasoline vehicles (Elser et al., 2018) that are regional or local. It is important to note that the other cations, such as magnesium, potassium, sodium, and calcium, can also contribute to aerosol neutralization. A previous offline filter-based study by (Pant et al., 2015) found metals like Cu, Zn, Pb, Cd, and As in the atmosphere of Delhi megacity. In a recent study (Rai et al., 2020), analyzed the real-time measurement of elemental composition during the winter period at IITD, which found that most of the metallic ions contribute to coarse mode PM_{10} particles (aerodynamic

diameter less than $10 \mu\text{m}$). Another study (Rai et al., 2021) has found the PM_{10} concentration at IITD is significantly higher than the cities like Beijing, Krakow, and London. As most of these metallic ions contribute to coarse mode particles, our assumption of dominant neutralization from ammonium is reasonable.

Diurnal mean and standard deviations of ANRs that derived from the peak fitted HR-MS inorganic species show that the aerosols at MRIU are more neutralized than that of IITD (Fig. 5a). This neutralized pattern at MRIU is more dominant during photochemically active periods (PAPs, Fig. 5a) and observed to have a higher midnight ANR variability. This midnight variability could have resulted from the difference in the individual inorganic species contribution towards the total PM_1 mass at this peak hour. IITD contrarily shows an ANR less than one, indicates that the aerosols are not completely neutralized and are acidic, which, in turn, can affect the aerosol's growth pattern there. Both MRIU and IITD show a relative increase in the ANR values during the daytime that peaked around noon that indicates the increased neutralization at this period (Fig. 4a).

To understand the size-dependent contributions of aerosols towards these ANRs, we have calculated size-resolved ANR (Qi Zhang et al., 2007) at these two sites (Fig. 5b and c) from a d_{va} of ~ 100 nm– 1200 nm. The ANRs at bins below MBDs of 108 and 118 nm at IITD and MRIU respectively and above 800 nm at both sites have not been used for the discussion here due to their 1) low S/N ratios in these lower bins and 2), to have a better comparison of ANR variations over the similar size range. Diurnal bin-wise increase in ANR is more distinct at IITD that shows a clear increase during PAP. This distinct increase of bin-wise ANR values during PAP is absent in the case of MRIU and show a

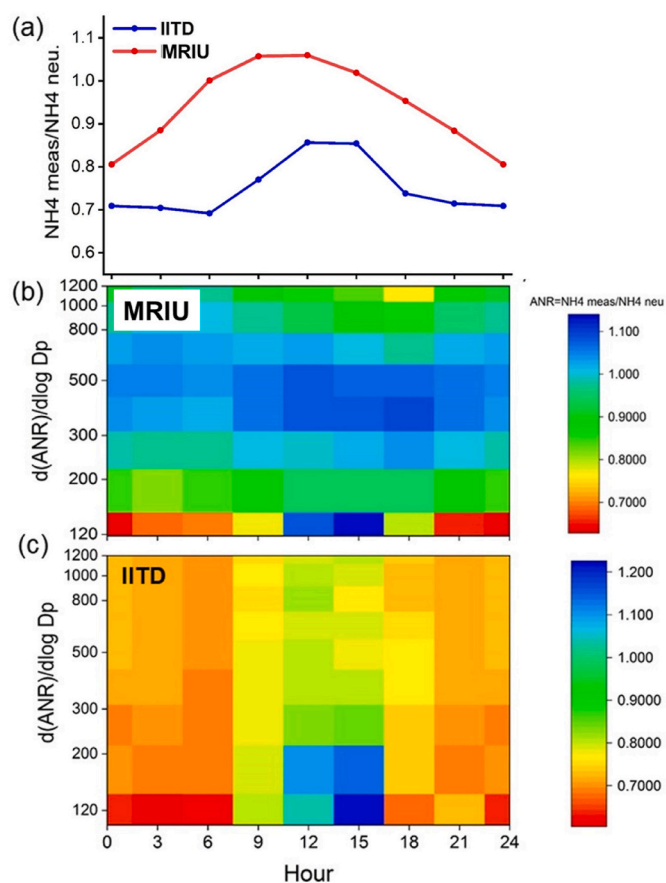


Fig. 5. 3-hour averaged size-resolved aerosol ANRs at two sites using high-resolution data. (a) Indicates the diurnal aerosol acidity from MS data (b) and (c) indicate the size-resolved aerosol acidity from HR-PTof data at MRIU and IITD, respectively.

uniform bin-wise ANR values throughout the day. The lower diameter particles with MBD less than 177 nm are not completely neutralized and acidic, while the higher size particles (>177 nm) are generally neutralized at MRIU (Fig. 5b). It is important to note that the increase in ANR during 12:00–15:00 LT in the size bin with MBD of 118 nm at MRIU is mainly due to the low molar concentrations of chloride and nitrate, which is well neutralized by the high molar concentrations of ammonium during these afternoon periods (Fig. S14b). However, in general, this size-dependent variation in acidity is not present at IITD (Fig. 5c) that observed to have higher, uniform acidity over a broader size range of aerosols (D_{va} ~200–800 nm). At IITD, high acidity in aerosols

promotes the acid-catalyzed SOA productions (Qi Zhang et al., 2007) over the broader size bins. These SOA productions lead to an increase in the hygroscopicity of aerosols (Jimenez et al., 2009), which makes the IITD environment more growth-promoting than MRIU. The representative size distributions of the stacked molar concentration of anions with the neutralizing cations (solid lines) indicating that the aerosols are not neutralized in midnight as well as noon at IITD (Figs. S7c and d), while in case of MRIU, these anions are neutralized with the counter cations (Figs. S7a and b). Additionally, the apparent overnight acidity can have interference from the 1) uncertainties and biases in relative ionization efficiencies (RIE) 2) organonitrates and organosulfates.

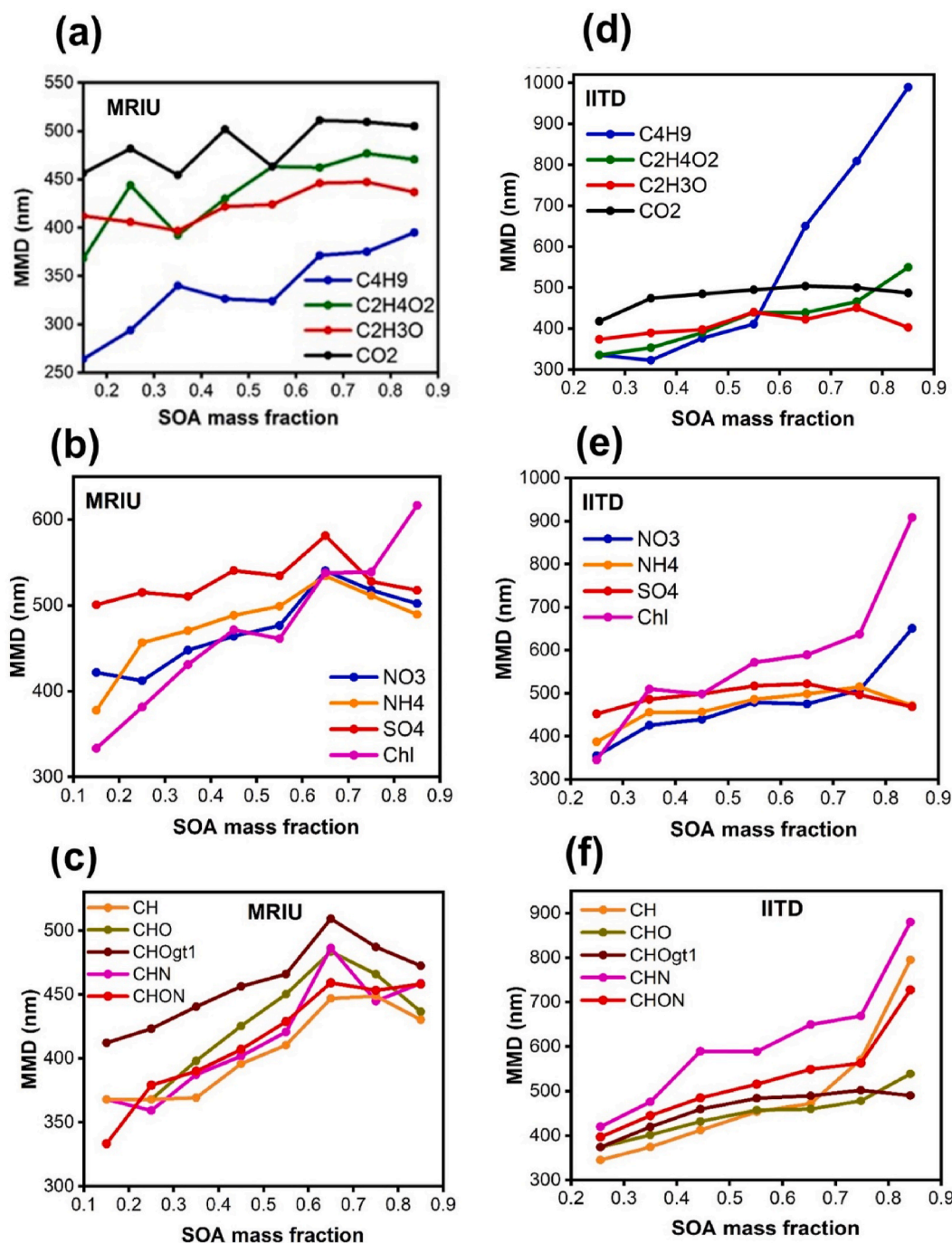


Fig. 6. Variation in the mean modal diameters (MMDs) of organic proxies, inorganics, and organic families with respect to the increase in the mass fraction of secondary organic aerosols (SOA). The variation of MMDs of organic proxies, inorganics, and organic families are shown in Fig. 6a, b, and 6c for MRIU, and 6 d, 6e, and 6f for IITD, respectively.

3.5. Interactions of the sizes of OA sources, families, and inorganics with the mass fraction of SOA

To understand the bin-wise growth mechanism of OA and inorganics better, the SOA mass fraction is plotted against the sizes of these species at each site (Fig. 6a–f). Sum of the MFs of secondary PMF factors (SVOOA-1, SVOOA-2, and LVOOA) are used to calculate the SOA mass fraction (MF_{SOA}). The MMDs of HR OA proxies, families, and inorganics over a 0.1 increment in the MF_{SOA} is termed as MMD_{SOA} at each site (Fig. 6a–f). 3-hour averaged MF_{SOA} is binned at a step size of 0.1 and arranged in ascending order at IITD (from 0.2 to 0.9) and MRIU (from 0.1 to 0.9) and is compared with the corresponding MMD_{SOA} of OA proxies, families and inorganics. To understand the growth, the MMD_{SOA} of these species corresponds to an increase in MF_{SOA} from minimum to maximum value are discussed in the following section.

At both sites, the MMD_{SOA} of the primary OA proxies such as $C_4H_9^+$ and $C_2H_4O_2^+$ show an increase in size with the increase in MF_{SOA} (Fig. 6a (MRIU) and d (IITD)). HOA proxy, $C_4H_9^+$, grows more distinctly at IITD (from an MMD_{SOA} ~330–~990 nm) than that of MRIU (from an MMD_{SOA} ~260–~370 nm), corresponds to an increase in MF_{SOA} from minimum to a maximum value. Similarly, biomass proxy ($C_2H_4O_2^+$) shows a notable growth (from ~335 to ~550 nm) at IITD than that of MRIU (~370–~470 nm). This positive correlation between MF_{SOA} and MMD_{SOA} is not seen in the case of secondary HR proxy fragments such as $C_2H_3O^+$ and CO_2^+ , indicating that the sizes of these proxies were not affected by the increase in MF_{SOA} .

Inorganic chloride shows significant growth at both the sites (~330–620 nm at MRIU and ~354–900 nm at IITD) that followed by nitrate (~420–500 nm at MRIU and ~350–650 nm at IITD) and NH_4^+ (~380–490 nm at MRIU and ~390–470 nm at IITD), (Fig. 6b and e). The growth of organic families corresponds to the increase in MF_{SOA} at both sites is shown in Fig. 6c, and f. All organic families show growth corresponds to an increase in the MF_{SOA} from minimum to maximum. Among these, CH, CHO, CHN, and CHON families show more distinct growth than other organic families. Growth of these organic families corresponds to the minimum to maximum MF_{SOA} are CH (~370–430 nm at MRIU and ~340–790 nm at IITD), CHO (~370–440 nm at MRIU and ~374–540 nm at IITD), CHN (~370–460 nm at MRIU and ~420–880 nm at IITD) and, CHON (~330–460 nm at MRIU and ~400–730 nm at IITD).

Growth of the primary OA proxies, families (CH, CHO, and amines) and inorganic species provide new insights towards the growth of the primary non-refractory species in NCR. The simultaneous growth of HOA ($C_4H_9^+$) with CH, amines, and chloride indicate that most of these aerosols follow a similar evolution mechanism in the atmosphere, that promotes the internal mixing of these species during some phase of their evolution. We have tried to quantify the approximate growth rate of organic and inorganic species at NCR in accordance with the increase in MF_{SOA} . The growth rates of species are discussed here as the growth rate in nm per 10 percentage increase in MF_{SOA} and indicated as GR_{10} . The GR_{10} for different species is discussed for MRIU and IITD, respectively, in the following discussion. Among various species, HOA (GR_{10} ~13 and 93 nm), BBOA (GR_{10} ~12 and 31 nm), chloride (GR_{10} ~35 nm and 80 nm), Nitrate (GR_{10} ~10 nm and 42 nm), CH family (GR_{10} ~8 nm and 64 nm), CHO family (GR_{10} ~8 nm and 24 nm), CHN family (GR_{10} ~11 nm and 66 nm) and CHON family (GR_{10} ~16 nm and 47 nm) show distinct growth with MF_{SOA} .

The growth patterns of OA species and inorganics are correlated with their possible mixing state at two sites in NCR. At both NCR sites, POA proxies show distinctly different diameters with CO_2^+ (Fig. 3a and d) at peak emission period (18:00–21:00 LT), indicate that the aerosols are externally mixed. The concurrent growth of HOA with CH and amine families and chloride at both sites indicate their internal mixing in NCR. As discussed in earlier sections, the growth-promoting factors at IITD, such as higher vehicular intensity and heterogeneity, acidity, RH, and lens diameter than that of MRIU promote the growth of aerosols

distinctly there. The evolution of the size of the fine OA and inorganics show that they significantly depend on the SOA MF at IITD and MRIU.

A major part of the growths of HOA at NCR sites can be explained by the considerably high condensable species concentrations in IGP sites such as Delhi (Kulmala et al., 2005) and Kanpur (Kanawade et al., 2014) when compared to the less polluted environments. Also, anthropogenic emissions add to the condensation sink. In IGP, this condensation sink from pre-existing particles is known to suppress particle nucleation (Kanawade et al., 2014). This indicates that the OOA condensation significantly determining the particle growth at MRIU than in IITD. At IITD, along with OOA condensation, coagulation (Gani et al., 2020) and the introduction of higher diameter HOA at the vicinity is contributing to the shifting of HOA towards the higher diameter in the daytime.

Along with condensation, coagulation is also an important growth driving mechanism in Delhi megacity (Gani et al., 2020). found that the rapid coagulation of ultrafine particles is prominent during periods with high accumulation mode particle concentrations. One-hour coagulation scavenging removes ~10% of 100 nm diameter particles present initially. The coagulation sinks for ultrafine particles in Delhi is ~20 times larger than a clean city like Helsinki. In polluted periods, when prominent concentrations of particles are in accumulation mode (which results in high surface area concentrations), the concentrations of ultrafine particles are suppressed by the rapid coagulation sink (Gani et al., 2020).

4. Conclusions

NCR receives OA and inorganics from complex sources with different atmospheric processing. The climatological interferences of these fine particulate matter (PM) in NCR is significantly depending on their evolution in size and composition. In the present study, we have applied the recently reported HR-PTof analysis at two sites in NCR, to meticulously understand the size evolutions of fine particulate matter and the factors that influence it.

Our study finds that the Primary and secondary OA proxies show distinct diurnal growth at both sites in NCR, and secondary OA proxies do not show notable variations in the MMDs. At both NCR sites, amines, chloride, and hydrocarbon like OA (HOA) show similar diurnal growth and possibilities of internal mixing.

HOA, families of hydrocarbon (CH), and amines and chloride grow prominently up to a diameter of ~900 nm during the photochemically active period at IITD. The growth of HOA significantly depends on the HOA/SFC ratio at both sites.

Sampling sites in Delhi show a significant difference in size-resolved acidity that contributes towards the distinct growth of species there. Aerosols at MRIU is more neutralized (Acid Neutralization Ratio (ANR) ~1) than that of IITD (ANR ~0.75). Secondary OA (SOA) significantly promotes the growth of primary OA sources, OA families, and inorganics such as chloride and nitrate. For 0.1 (MF) increase in SOA, the sizes of HOA, chloride, primary CH family and amines (CHN family), and secondary amines (CHON family) are increased by ~93, 80, 64, 66, and 47 nm at IITD and ~14, 35, 8, 11, and 16 nm at MRIU respectively. Condensation of SOA can be the key growth mechanism at both sites of NCR.

Our study indicates the prevailing local conditions of high vehicular density and heterogeneity, and the presence of growth-promoting factors such as acidity and RH conditions significantly affect the growth of fine particulate matter there. Models need to incorporate this change in the growth patterns due to the prevailing local conditions for the better prediction of atmospheric evolution.

CRedit authorship contribution statement

Navaneeth Meena Thamban: Methodology, Software, Validation, Formal analysis, Investigation, Writing – original draft, Writing – review & editing, Visualization. **Vipul Lalchandani:** Investigation,

Methodology, Formal analysis, Investigation, Writing – review & editing. **Varun Kumar:** Investigation, Methodology, Formal analysis, Investigation, Writing – review & editing. **Suneeti Mishra:** Investigation, Writing – review & editing. **Deepika Bhattu:** Investigation, Methodology, Writing – review & editing. **Jay G. Slowik:** Investigation, Methodology, Writing – review & editing. **Andre S.H. Prevot:** Writing – review & editing, Project administration, Funding acquisition. **Rangu Satish:** Investigation, Methodology, Writing – review & editing. **Neeraj Rastogi:** Writing – review & editing, Project administration, Funding acquisition. **Sachchida N. Tripathi:** Writing – review & editing, Supervision, Project administration, Funding acquisition.

Declaration of competing interest

The authors declare that they have no known competing financial interests or personal relationships that could have appeared to influence the work reported in this paper.

Acknowledgment

First author and corresponding authors acknowledge the help and support from Shashi Tiwari and Manav Rachna International University, Faridabad, India during this work. The corresponding authors gratefully acknowledges the financial support provided by the Department of Biotechnology (DBT), Government of India, to conduct this research under grant no. BT/IN/UK/APHH/41/KB/2016-17 dated 19th July 2017 and financial support provided by Central Pollution control board (CPCB), Government of India, to conduct this research under grant no. AQM/Source apportionment_EPC Project/2017. We also acknowledge the contribution by the Swiss National Science Foundation projects 200021_169787, 200020_188624, IZLCZ2_169986.

Appendix A. Supplementary data

Supplementary data to this article can be found online at <https://doi.org/10.1016/j.atmosenv.2021.118752>.

References

- Aiken, A.C., Decarlo, P.F., Kroll, J.H., Worsnop, D.R., Huffman, J.A., Docherty, K.S., Ulbrich, I.M., Mohr, C., Kimmel, J.R., Sueper, D., Sun, Y., Zhang, Q., Trimborn, A., Northway, M., Ziemann, P.J., Canagaratna, M.R., Onasch, T.B., Alfarra, M.R., Prevot, A.S.H., Dommen, J., Duplissy, J., Metzger, A., Baltensperger, U., Jimenez, J.L., 2008. O/C and OM/OC ratios of primary, secondary, and ambient organic aerosols with high-resolution time-of-flight aerosol mass spectrometry. *Environ. Sci. Technol.* 42, 4478–4485. <https://doi.org/10.1021/es703009q>.
- Albrecht, B.A., 1989. Aerosols, cloud microphysics, and fractional cloudiness. *Science* 84, 1227–1230. <https://doi.org/10.1126/science.245.4923.1227>.
- Alfarra, M.R., Prevot, A.S.H., Szidat, S., Sandradewi, J., Weimer, S., Lanz, V.A., Schreiber, D., Mohr, M., Baltensperger, U., 2007. Identification of the mass spectral signature of organic aerosols from wood burning emissions. *Environ. Sci. Technol.* 41, 5770–5777. <https://doi.org/10.1021/es062289b>.
- Allan, J.D., Jimenez, J.L., Williams, P.I., Alfarra, M.R., Bower, K.N., Jayne, J.T., Coe, H., Worsnop, D.R., Rami Alfarra, M., Bower, K.N., Jayne, J.T., Coe, H., Worsnop, D.R., Jimenez, J.L., Williams, P.I., Alfarra, M.R., Bower, K.N., Jayne, J.T., Coe, H., Worsnop, D.R., 2003. Quantitative sampling using an Aerodyne aerosol mass spectrometer 1. Techniques of data interpretation and error analysis. *J. Geophys. Res.* Atmos. 108. <https://doi.org/10.1029/2002jd002358> n/a-n/a.
- Bhattu, D., Tripathi, S.N., 2015. CCN closure study: effects of aerosol chemical composition and mixing state. *J. Geophys. Res.* 120, 766–783. <https://doi.org/10.1002/2014JD021978>.
- Bikkina, S., Andersson, A., Kirillova, E.N., Holmstrand, H., Tiwari, S., Srivastava, A.K., Bisht, D.S., Gustafsson, O., 2019. Air quality in megacity Delhi affected by countryside biomass burning. *Nat. Sustain.* 2, 200–205. <https://doi.org/10.1038/s41893-019-0219-0>.
- Bozzetti, C., Daellenbach, K.R., Hueglin, C., Fermo, P., Sciare, J., Kasper-Giebl, A., Mazar, Y., Abbaszade, G., El Kazzi, M., Gonzalez, R., Shuster-Meiseles, T., Flasch, M., Wolf, R., Krepelová, A., Canonaco, F., Schnelle-Kreis, J., Slowik, J.G., Zimmermann, R., Rudich, Y., Baltensperger, U., El Haddad, I., Prévôt, A.S.H., 2016. Size-resolved identification, characterization, and quantification of primary biological organic aerosol at a European rural site. *Environ. Sci. Technol.* 50, 3425–3434. <https://doi.org/10.1021/acs.est.5b05960>.
- Canagaratna, M.R., Jayne, J.T., Ghertner, D.A., Herndon, S., Shi, Q., Jimenez, J.L., Silva, P.J., Williams, P., Lanni, T., Drewnick, F., Demerjian, K.L., Kolb, C.E., Worsnop, D.R., 2004. Chase studies of particulate emissions from in-use New York City vehicles. *Aerosol. Sci. Technol.* 38, 555–573. <https://doi.org/10.1080/02786820490465504>.
- Canagaratna, M.R., Jayne, J.T., Jimenez, J.L., Allan, J.D., Alfarra, M.R., Zhang, Q., Onasch, T.B., Drewnick, F., Coe, H., Middlebrook, A., Delia, A., Williams, L.R., Trimborn, A.M., Northway, M.J., DeCarlo, P.F., Kolb, C.E., Davidovits, P., Worsnop, D.R., 2007. Chemical and microphysical characterization of ambient aerosols with the aerodyne aerosol mass spectrometer. *Mass Spectrom. Rev.* 26, 185–222. <https://doi.org/10.1002/mas.20115>.
- Canagaratna, M.R., Jimenez, J.L., Kroll, J.H., Chen, Q., Kessler, S.H., Massoli, P., Hildebrandt Ruiz, L., Fortner, E., Williams, L.R., Wilson, K.R., Surratt, J.D., Donahue, N.M., Jayne, J.T., Worsnop, D.R., 2015. Elemental ratio measurements of organic compounds using aerosol mass spectrometry: characterization, improved calibration, and implications. *Atmos. Chem. Phys.* 15, 253–272. <https://doi.org/10.5194/acp-15-253-2015>.
- Canonaco, F., Crippa, M., Slowik, J.G., Baltensperger, U., Prévôt, A.S.H., 2013. SoFi, an IGOR-based interface for the efficient use of the generalized multilinear engine (ME-2) for the source apportionment: ME-2 application to aerosol mass spectrometer data. *Atmos. Meas. Tech.* 6, 3649–3661. <https://doi.org/10.5194/amt-6-3649-2013>.
- Cappa, C.D., Jimenez, J.L., 2010. Quantitative estimates of the volatility of ambient organic aerosol. *Atmos. Chem. Phys.* 10, 5409–5424. <https://doi.org/10.5194/acp-10-5409-2010>.
- Chakraborty, A., Bhattu, D., Gupta, T., Tripathi, S.N., Canagaratna, M.R., 2015. Real-time measurements of ambient aerosols in a polluted Indian city: sources, characteristics, and processing of organic aerosols during foggy and nonfoggy periods. *J. Geophys. Res.* 120, 9006–9019. <https://doi.org/10.1002/2015JD023419>.
- Chien, S.M., Huang, Y.J., 2010. Sizes and polycyclic aromatic hydrocarbon composition distributions of nano, ultrafine, fine, and coarse particulates emitted from a four-stroke motorcycle. *J. Environ. Sci. Heal. - Part A Toxic/Hazardous Subst. Environ. Eng.* 45, 1768–1774. <https://doi.org/10.1080/10934529.2010.513289>.
- Chowdhury, S., Dey, S., Tripathi, S.N., Beig, G., Mishra, A.K., Sharma, S., 2017. “Traffic intervention” policy fails to mitigate air pollution in megacity Delhi. *Environ. Sci. Pol.* 74, 8–13. <https://doi.org/10.1016/j.envsci.2017.04.018>.
- DeCarlo, P.F., Kimmel, J.R., Trimborn, A., Northway, M.J., Jayne, J.T., Aiken, A.C., Gonin, M., Fuhrer, K., Horvath, T., Docherty, K.S., Worsnop, D.R., Jimenez, J.L., 2006. Field-deployable, high-resolution, time-of-flight aerosol mass spectrometer. *Anal. Chem.* 78, 8281–8289. <https://doi.org/10.1021/ac061249n>.
- DeCarlo, P.F., Slowik, J.G., Worsnop, D.R., Davidovits, P., Jimenez, J.L., 2004. Particle morphology and density characterization by combined mobility and aerodynamic diameter measurements. Part 1: Theory. *Aerosol Sci. Technol.* 38, 1185–1205. <https://doi.org/10.1080/027868290903907>.
- Decarlo, P.F., Ulbrich, I.M., Crouse, J., De Foy, B., Dunlea, E.J., Aiken, A.C., Knapp, D., Weinheimer, A.J., Campos, T., Wennberg, P.O., Jimenez, J.L., 2010. Investigation of the sources and processing of organic aerosol over the Central Mexican Plateau from aircraft measurements during MILAGRO. *Atmos. Chem. Phys.* 10, 5257–5280. <https://doi.org/10.5194/acp-10-5257-2010>.
- Douglas Goetz, J., Giordano, M.R., Stockwell, C.E., Christian, T.J., Maharjan, R., Adhikari, S., Bhawe, P.V., Praveen, P.S., Panday, A.K., Jayarathne, T., Stone, E.A., Yokelson, R.J., Decarlo, P.F., 2018. Speciated online PM1 from South Asian combustion sources-Part 1: fuel-based emission factors and size distributions. *Atmos. Chem. Phys.* 18, 14653–14679. <https://doi.org/10.5194/acp-18-14653-2018>.
- Draxler, R., Stunder, B., Rolph, G., Stein, A., Taylor, A., 2016. HYSPLIT4 User's Guide Version 4.248.
- Drinovec, L., Močnik, G., Zotter, P., Prévôt, A.S.H., Ruckstuhl, C., Coz, E., Rupakheti, M., Sciare, J., Müller, T., Wiedensohler, A., Hansen, A.D.A., 2015. The “dual-spot” Aethalometer: an improved measurement of aerosol black carbon with real-time loading compensation. *Atmos. Meas. Tech.* 8, 1965–1979. <https://doi.org/10.5194/amt-8-1965-2015>.
- Dusek, U., Frank, G.P., Hildebrandt, L., Curtius, J., Schneider, J., Walter, S., Chand, D., Drewnick, F., Hings, S., Jung, D., Borrmann, S., Andreae, M.O., 2006. Size matters more than chemistry for cloud-nucleating ability of aerosol particles. *Science* 84, 1375–1378. <https://doi.org/10.1126/science.1125261>.
- Elser, M., El-Haddad, I., Maasikets, M., Bozzetti, C., Wolf, R., Ciarelli, G., Slowik, J.G., Richter, R., Teinmaa, E., Hüglin, C., Baltensperger, U., Prévôt, A.S.H., 2018. High contributions of vehicular emissions to ammonia in three European cities derived from mobile measurements. *Atmos. Environ.* 175, 210–220. <https://doi.org/10.1016/j.atmosenv.2017.11.030>.
- Gani, S., Bhandari, S., Patel, K., Seraj, S., Soni, P., Arub, Z., Habib, G., Hildebrandt Ruiz, L., Apte, J.S., 2020. Particle number concentrations and size distribution in a polluted megacity: the Delhi Aerosol Supersite study. *Atmos. Chem. Phys.* 20, 8533–8549. <https://doi.org/10.5194/acp-20-8533-2020>.
- Gani, S., Bhandari, S., Seraj, S., Wang, D.S., Patel, K., Soni, P., Arub, Z., Habib, G., Hildebrandt Ruiz, L., Apte, J.S., 2019. Submicron aerosol composition in the world's most polluted megacity: the Delhi Aerosol Supersite study. *Atmos. Chem. Phys.* 19, 6843–6859. <https://doi.org/10.5194/acp-19-6843-2019>.
- Gaur, A., Tripathi, S.N., Kanawade, V.P., Tare, V., Shukla, S.P., 2014. Four-year measurements of trace gases (SO₂, NO_x, CO, and O₃) at an urban location, Kanpur, in Northern India. *J. Atmos. Chem.* 71, 283–301. <https://doi.org/10.1007/s10874-014-9295-8>.
- Goel, V., Hazarika, N., Kumar, M., Singh, V., Thamban, N.M., Tripathi, S.N., 2021. Variations in Black Carbon concentration and sources during COVID-19 lockdown in Delhi. *Chemosphere* 270, 129435. <https://doi.org/10.1016/j.chemosphere.2020.129435>.
- Goldstein, A.H., Worton, D.R., Williams, B.J., Hering, S.V., Kreisberg, N.M., Panić, O., Górecki, T., 2008. Thermal desorption comprehensive two-dimensional gas

- chromatography for in-situ measurements of organic aerosols. *J. Chromatogr. A* 1186, 340–347. <https://doi.org/10.1016/j.chroma.2007.09.094>.
- Griggs, D.J., Nogueir, M., 2002. Climate change 2001: the scientific basis. Contribution of working group I to the third assessment report of the intergovernmental panel on climate change. *Weather* 57, 267–269. <https://doi.org/10.1256/004316502320517344>.
- Hallquist, M., Wenger, J.C., Baltensperger, U., Rudich, Y., Simpson, D., Claeys, M., Dommen, J., Donahue, N.M., George, C., Goldstein, A.H., Hamilton, J.F., Herrmann, H., Hoffmann, T., Iinuma, Y., Jang, M., Jenkin, M.E., Jimenez, J.L., Kiendler-Scharr, A., Maenhaut, W., McFiggans, G., Mentel, T.F., Monod, A., Prévôt, A.S.H., Seinfeld, J.H., Surratt, J.D., Szmigielski, R., Wildt, J., 2009. The formation, properties and impact of secondary organic aerosol: current and emerging issues. *Atmos. Chem. Phys.* 9, 5155–5236. <https://doi.org/10.5194/acp-9-5155-2009>.
- Holt, K.E., 1961. Third interim report. *J. AOAC Int.* 44, 567–569. <https://doi.org/10.1093/jaoac/44.3.567>.
- Jacobson, M.Z., 2001. Strong radiative heating due to the mixing state of black carbon in atmospheric aerosols. *Nature* 409, 695–697. <https://doi.org/10.1038/35055518>.
- Jain, S., Sharma, S.K., Mandal, T.K., Saxena, M., 2018. Source apportionment of PM10 in Delhi, India using PCA/APCS, UNMIX and PMF. *Particuology* 37, 107–118. <https://doi.org/10.1016/j.partic.2017.05.009>.
- Jimenez, J.L., Canagaratna, M.R., Donahue, N.M., Prevot, A.S.H., Zhang, Q., Kroll, J.H., DeCarlo, P.F., Allan, J.D., Coe, H., Ng, N.L., Aiken, A.C., Docherty, K.S., Ulbrich, I. M., Grieshop, A.P., Robinson, A.L., Duplissy, J., Smith, J.D., Wilson, K.R., Lanz, V.A., Hueglin, C., Sun, Y.L., Tian, J., Laaksonen, A., Raatikainen, T., Rautiainen, J., Vaattovaara, P., Ehni, M., Kulmala, M., Tomlinson, J.M., Collins, D.R., Cubison, M.J., Dunlea, E.J., Huffman, J.A., Onasch, T.B., Alfarra, M.R., Williams, P.I., Bower, K., Kondo, Y., Schneider, J., Drewnick, F., Borrmann, S., Weimer, S., Demerjian, K., Salcedo, D., Cottrell, L., Griffin, R., Takami, A., Miyoshi, T., Hatakeyama, S., Shimono, A., Sun, J.Y., Zhang, Y.M., Dzepina, K., Kimmel, J.R., Sueper, D., Jayne, J. T., Herndon, S.C., Trimborn, A.M., Williams, L.R., Wood, E.C., Middlebrook, A.M., Kolb, C.E., Baltensperger, U., Worsnop, D.R., 2009. Evolution of organic aerosols in the atmosphere. *Science* 326, 1525–1529. <https://doi.org/10.1126/science.1180353>.
- Kanawade, V.P., Tripathi, S.N., Siingh, D., Gautam, A.S., Srivastava, A.K., Kamra, A.K., Soni, V.K., Sethi, V., 2014. Observations of new particle formation at two distinct Indian subcontinental urban locations. *Atmos. Environ.* 96, 370–379. <https://doi.org/10.1016/j.atmosenv.2014.08.001>.
- Kaskaoutis, D.G., Sinha, P.R., Vojin, V., Kosmopoulos, P.G., Tripathi, S.N., Misra, A., Sharma, M., Singh, R.P., 2013. Aerosol properties and radiative forcing over Kanpur during severe aerosol loading conditions. *Atmos. Environ.* 79, 7–19. <https://doi.org/10.1016/j.atmosenv.2013.06.020>.
- Kulmala, M., Petäjä, T., Mönkkönen, P., Koponen, I.K., Dal Maso, M., Aalto, P.P., Lehtinen, K.E.J., Kerminen, V.M., 2005. On the growth nucleation mode particles: source rates of condensable vapor in polluted and clean environments. *Atmos. Chem. Phys.* 5, 409–416. <https://doi.org/10.5194/acp-5-409-2005>.
- Kumar, B., Chakraborty, A., Tripathi, S.N., Bhattu, D., 2016a. Highly time resolved chemical characterization of submicron organic aerosols at a polluted urban location. *Environ. Sci. Process. Impacts* 18, 1285–1296. <https://doi.org/10.1039/c6em00392c>.
- Kumar, S., Dey, S., Srivastava, A., 2016b. Quantifying enhancement in aerosol radiative forcing during “extreme aerosol days” in summer at Delhi National Capital Region, India. *Sci. Total Environ.* 550, 994–1000. <https://doi.org/10.1016/j.scitotenv.2016.01.191>.
- Lalchandani, V., Kumar, V., Tobler, A., Thamban, N.M., Mishra, S., Slowik, J.G., Bhattu, D., Rai, P., Satish, R., Ganguly, D., Tiwari, S.S.S., Rastogi, N., Tiwari, S.S.S., Mocnik, G., Prévôt, A.S.H., Tripathi, S.N., 2021. Real-time characterization and source apportionment of fine particulate matter in the Delhi megacity area during late winter. *Sci. Total Environ.* 770, 145324. <https://doi.org/10.1016/j.scitotenv.2021.145324>.
- Lanz, V.A., Alfarra, M.R., Baltensperger, U., Buchmann, B., Hueglin, C., Prévôt, A.S.H., 2007. Source apportionment of submicron organic aerosols at an urban site by factor analytical modelling of aerosol mass spectra. *Atmos. Chem. Phys.* 7, 1503–1522. <https://doi.org/10.5194/acp-7-1503-2007>.
- Manchanda, C., Kumar, M., Singh, V., Faisal, M., Hazarika, N., Shukla, A., Lalchandani, V., Goel, V., Thamban, N., Ganguly, D., Tripathi, S.N., 2021. Variation in chemical composition and sources of PM2.5 during the COVID-19 lockdown in Delhi. *Environ. Int.* 153, 106541. <https://doi.org/10.1016/j.envint.2021.106541>.
- Middlebrook, A.M., Bahreini, R., Jimenez, J.L., Canagaratna, M.R., 2012. Evaluation of composition-dependent collection efficiencies for the Aerodyne aerosol mass spectrometer using field data. *Aerosol Sci. Technol.* 46, 258–271. <https://doi.org/10.1080/02786826.2011.620041>.
- Mohr, C., DeCarlo, P.F., Hering, M.F., Chirico, R., Slowik, J.G., Richter, R., Reche, C., Alastuey, A., Querol, X., Seco, R., Penuelas, J., Jimenez, J.L., Crippa, M., Zimmermann, R., Baltensperger, U., Prévôt, A.S.H., 2012. Identification and quantification of organic aerosol from cooking and other sources in Barcelona using aerosol mass spectrometer data. *Atmos. Chem. Phys.* 12, 1649–1665. <https://doi.org/10.5194/acp-12-1649-2012>.
- Mohr, C., Huffman, J.A., Cubison, M.J., Aiken, A.C., Docherty, K.S., Kimmel, J.R., Ulbrich, I.M., Hannigan, M., Jimenez, J.L., 2009. Characterization of primary organic aerosol emissions from meat cooking, trash burning, and motor vehicles with high-resolution aerosol mass spectrometry and comparison with ambient and chamber observations. *Environ. Sci. Technol.* 43, 2443–2449. <https://doi.org/10.1021/es8011518>.
- Moteki, N., Kondo, Y., 2010. Dependence of laser-induced incandescence on physical properties of black carbon aerosols: measurements and theoretical interpretation. *Aerosol Sci. Technol.* 44, 663–675. <https://doi.org/10.1080/02786826.2010.484450>.
- Moteki, N., Kondo, Y., 2007. Effects of mixing state on black carbon measurements by laser-induced incandescence. *Aerosol Sci. Technol.* 41, 398–417. <https://doi.org/10.1080/02786820701199728>.
- Ng, N.L., Canagaratna, M.R., Zhang, Q., Jimenez, J.L., Tian, J., Ulbrich, I.M., Kroll, J.H., Docherty, K.S., Chhabra, P.S., Bahreini, R., Murphy, S.M., Seinfeld, J.H., Hildebrandt, L., Donahue, N.M., Decarlo, P.F., Lanz, V.A., Prévôt, A.S.H., Dinar, E., Rudich, Y., Worsnop, D.R., 2010. Organic aerosol components observed in northern hemispheric datasets from aerosol mass spectrometry. *Atmos. Chem. Phys.* 10, 4625–4641. <https://doi.org/10.5194/acp-10-4625-2010>.
- Paatero, P., Tapper, U., 1994. Positive matrix factorization: a non-negative factor model with optimal utilization of error estimates of data values. *Environmetrics* 5, 111–126. <https://doi.org/10.1002/env.3170050203>.
- Pant, P., Shukla, A., Kohl, S.D., Chow, J.C., Watson, J.G., Harrison, R.M., 2015. Characterization of ambient PM2.5 at a pollution hotspot in New Delhi, India and inference of sources. *Atmos. Environ.* 109, 178–189. <https://doi.org/10.1016/j.atmosenv.2015.02.074>.
- Rai, P., Furger, M., Slowik, J.G., Canonaco, F., Fröhlich, R., Hüglin, C., Minguillón, M.C., Pettersson, K., Baltensperger, U., Prévôt, A.S.H., 2020. Source apportionment of highly time-resolved elements during a firework episode from a rural freeway site in Switzerland. *Atmos. Chem. Phys.* 20, 1657–1674. <https://doi.org/10.5194/acp-20-1657-2020>.
- Rai, P., Slowik, J.G., Furger, M., El Haddad, I., Visser, S., Tong, Y., Singh, A., Wehrle, G., Kumar, V., Tobler, A.K., Bhattu, D., Wang, L., Ganguly, D., Rastogi, N., Huang, R.-J., Necki, J., Cao, J., Tripathi, S.N., Baltensperger, U., Prévôt, A.S.H., 2021. Highly time-resolved measurements of element concentrations in PM10 and PM2.5: comparison of Delhi, Beijing, London, and Krakow. *Atmos. Chem. Phys.* 21, 717–730. <https://doi.org/10.5194/acp-21-717-2021>.
- Satish, R., Shamjad, P., Thamban, N., Tripathi, S., Rastogi, N., 2017. Temporal characteristics of Brown carbon over the central Indo-Gangetic Plain. *Environ. Sci. Technol.* 51, 6765–6772. <https://doi.org/10.1021/acs.est.7b00734>.
- Schwarz, J.P., Gao, R.S., Fahey, D.W., Thomson, D.S., Watts, L.A., Wilson, J.C., Reeves, J.M., Darbeheshti, M., Baumgardner, D.G., Kok, G.L., Chung, S.H., Schulz, M., Hendricks, J., Lauer, A., Kärcher, B., Slowik, J.G., Rosenlof, K.H., Thompson, T.L., Langford, A.O., Loewenstein, M., Aikin, K.C., 2006. Single-particle measurements of midlatitude black carbon and light-scattering aerosols from the boundary layer to the lower stratosphere. *J. Geophys. Res. Atmos.* 111, D16207. <https://doi.org/10.1029/2006JD007076>.
- Stanier, C.O., Khlystov, A.Y., Pandis, S.N., 2004. Ambient aerosol size distributions and number concentrations measured during the Pittsburgh Air Quality Study (PAQS). *Atmos. Environ.* 38, 3275–3284. <https://doi.org/10.1016/j.atmosenv.2004.03.020>.
- Stein, A.F., Draxler, R.R., Rolph, G.D., Stunder, B.J.B., Cohen, M.D., Ngan, F., 2015. NOAA's hybrid atmospheric transport and dispersion modeling system. *Bull. Am. Meteorol. Soc.* <https://doi.org/10.1175/BAMS-D-14-00110.1>.
- Stephens, M., Turner, N., Sandberg, J., 2003. Particle identification by laser-induced incandescence in a solid-state laser cavity. *Appl. Opt.* 42, 3726. <https://doi.org/10.1364/ao.42.003726>.
- Thamban, N.M., Joshi, B., Tripathi, S.N., Sueper, D., Canagaratna, M.R., Moosakutty, S. P., Satish, R., Rastogi, N., 2019. Evolution of aerosol size and composition in the Indo-Gangetic Plain: size-resolved analysis of high-resolution aerosol mass spectra. *ACS Earth Sp. Chem.* 3, 823–832. <https://doi.org/10.1021/acsearthspacechem.8b00207>.
- Thamban, N.M., Tripathi, S.N., Moosakutty, S.P., Kuntamukkala, P., Kanawade, V.P., 2017. Internally mixed black carbon in the Indo-Gangetic Plain and its effect on absorption enhancement. *Atmos. Res.* 197, 211–223. <https://doi.org/10.1016/j.atmosres.2017.07.007>.
- Ulbrich, I.M., Canagaratna, M.R., Zhang, Q., Worsnop, D.R., Jimenez, J.L., 2009. Interpretation of organic components from Positive Matrix Factorization of aerosol mass spectrometric data. *Atmos. Chem. Phys.* 9, 2891–2918. <https://doi.org/10.5194/acp-9-2891-2009>.
- Wang, L., Slowik, J., Tripathi, N., Bhattu, D., Rai, P., Kumar, V., Vats, P., Satish, R., Baltensperger, U., Ganguly, D., Rastogi, N., Sahu, L., Tripathi, S., Prévôt, A., 2020. Source characterization of volatile organic compounds measured by PTR-ToF-MS in Delhi, India. *Atmos. Chem. Phys.* 1–27. <https://doi.org/10.5194/acp-2020-11>.
- Weber, R.J., Guo, H., Russell, A.G., Nenes, A., 2016. High aerosol acidity despite declining atmospheric sulfate concentrations over the past 15 years. *Nat. Geosci.* 9, 282–285. <https://doi.org/10.1038/ngeo2665>.
- Williams, L.R., Gonzalez, L.A., Peck, J., Trimborn, D., McInnis, J., Farrar, M.R., Moore, K. D., Jayne, J.T., Robinson, W.A., Lewis, D.K., Onasch, T.B., Canagaratna, M.R., Trimborn, A., Timko, M.T., Magoon, G., Deng, R., Tang, D., De La Rosa Blanco, E., Prévôt, A.S.H., Smith, K.A., Worsnop, D.R., 2013. Characterization of an aerodynamic lens for transmitting particles greater than 1 micrometer in diameter into the Aerodyne aerosol mass spectrometer. *Atmos. Meas. Tech.* 6, 3271–3280. <https://doi.org/10.5194/amt-6-3271-2013>.
- Yang, H.H., Chien, S.M., Chao, M.R., Lin, C.C., 2005. Particle size distribution of polycyclic aromatic hydrocarbons in motorcycle exhaust emissions. *J. Hazard Mater.* 125, 154–159. <https://doi.org/10.1016/j.jhazmat.2005.05.019>.
- Zhang, Qi, Canagaratna, M.R., Jayne, J.T., Worsnop, D.R., Jimenez, J.L., 2005a. Time- and size-resolved chemical composition of submicron particles in Pittsburgh: implications for aerosol sources and processes. *J. Geophys. Res. Atmos.* 110, 1–19. <https://doi.org/10.1029/2004JD004649>.
- Zhang, Q., Jimenez, J.L., Canagaratna, M.R., Allan, J.D., Coe, H., Ulbrich, I., Alfarra, M. R., Takami, A., Middlebrook, A.M., Sun, Y.L., Dzepina, K., Dunlea, E., Docherty, K., DeCarlo, P.F., Salcedo, D., Onasch, T., Jayne, J.T., Miyoshi, T., Shimono, A., Hatakeyama, S., Takegawa, N., Kondo, Y., Schneider, J., Drewnick, F., Borrmann, S.,

- Weimer, S., Demerjian, K., Williams, P., Bower, K., Bahreini, R., Cottrell, L., Griffin, R.J., Rautiainen, J., Sun, J.Y., Zhang, Y.M., Worsnop, D.R., 2007a. Ubiquity and dominance of oxygenated species in organic aerosols in anthropogenically-influenced Northern Hemisphere midlatitudes. *Geophys. Res. Lett.* 34, L13801. <https://doi.org/10.1029/2007GL029979>.
- Zhang, Qi, Jimenez, J.L., Worsnop, D.R., Canagaratna, M., 2007b. A case study of urban particle acidity and its influence on secondary organic aerosol. *Environ. Sci. Technol.* 41, 3213–3219. <https://doi.org/10.1021/es061812j>.
- Zhang, Qi, Rami Alfarra, M., Worsnop, D.R., Allan, J.D., Coe, H., Canagaratna, M.R., Jimenez, J.L., 2005b. Deconvolution and quantification of hydrocarbon-like and oxygenated organic aerosols based on aerosol mass spectrometry. *Environ. Sci. Technol.* 39, 4938–4952. <https://doi.org/10.1021/es048568l>.
- Zhang, Q., Worsnop, D.R., Canagaratna, M.R., Jimenez, J.L., 2005. Hydrocarbon-like and oxygenated organic aerosols in Pittsburgh: insights into sources and processes of organic aerosols. *Atmos. Chem. Phys.* 5, 3289–3311. <https://doi.org/10.5194/acp-5-3289-2005>.